UiT The Arctic University of Norway
Faculty of Science and Technology
Department of Physics and Technology

Application of quantitative phase microscopy in micro-biology for label-free imaging of bacteria

Attiqa Abrar

FYS-3900 Masters Thesis in Physics March, 2022

Acknowledgment

I attended UiT-The Arctic University of Norway to pursue my master's degree in physics, and it was a fantastic experience. The Optical Nanoscopy research group at UiT's Department of Physics and Technology has always had a positive and welcoming culture. The group has been a fantastic location for both social and scientific activity. My master's thesis research was a collaborative effort, and I'd like to thank a few colleagues below for their contributions. —

- My supervisor is Professor Balpreet Singh Ahluwalia. He offered me the opportunity to work on this research, which allowed me to learn more about quantitative phase microscopy. Your regular oversight, as well as the key information given, are both important to appreciate.

- My co-supervisor, Azeem Ahmed. Under his tutelage, I made the initial steps toward QPM. Thank you for teaching me how to do experiments, and especially for motivating me to learn MATLAB. Our discussions were always uplifting, and your positivity inspired me to keep improving my experimental approaches. You also taught me a lot about presenting abilities. I owe you a huge debt of gratitude for guiding me through my master's thesis.

- I want to extend sincere thanks to my husband Hafiz Abrar anwar khan for his moral support. His constant support and motivation helped me to pursue my dream education. Finally, My parents owe me a debt of gratitude for giving me with a good education that served as a solid basis for my higher education and my brother Sheraz Javed for his strong support and trust.

March 14, 2022 *Attiqa Abrar*

Abstract

Bacteria are the planet's oldest and the most common life forms. Bacteria have developed alongside humans and are good and harmful to our health. Our bodies contain nearly ten times the number of bacteria as human cells, and this natural microbiota is critical for appropriate development, nutrition, and disease resistance. Unfortunately, we live in an environment rich with bacteria that may cause a wide range of human diseases.[1]

Antimicrobial resistance *(AMR)* occurs when bacteria no longer remain vulnerable to the antimicrobial for which it was responsive in the past. Around 33,000 Europeans die each year from infections caused by *(AMR)* bacteria [2]. However, this number will be ten times the current number of deaths by 2050 if *AMR* develops rapidly [2]. Furthermore, the lack of new antibiotics in the development or trial phases is causing concern, particularly for multi-drug resistant bacteria that manufacture extended spectrum beta-lactamase (ESBLs) and carbapenems. Enterobacteriaceae (*E. coli* and *Klebsiella pneumonia*) is a family of bacteria that belongs to the *WHO's* priority one pathogen list.[3]

In this thesis, we tried to see if it is possible to see the potential difference between an AMR and a *non-AMR* bacterium. Also, we want to explore if it is possible to visualize any difference between different *AMR* bacteria cells. And to see the bacteria, we need an imaging technique that is suitable for imaging at high speed without the need for labels. The next important fact is if the technique is quantitative, we might be able to see the difference in the quantitative parameters of the two types of bacteria cells. We had one such option in our laboratory as Quantitative phase microscopy *(QPM)*.

QPM is a non-contact, non-invasive, and label-free methodology that can quantify various morphological and statistical parameters such as refractive index, height, dry mass, surface area, volume, sphericity, mean associated with biological specimens.[4]

This thesis aims to obtain *QPM* images of three different bacteria species: *E. coli*, *Klebsiella pneumonia (K. pneumonia)*, and *Staphylococcus aureus (S. aureus)*. The *E. coli* bacteria have two different strains: *E. coli(CCUG17620 and NCTC13441)*. One of them is the wild type without an antimicrobial resistance gene, and the other is the non-wild type with an AMR gene and, in this case, will be an extended-spectrum beta-lactamase *ESBLs*. Except for one bacteria sample, all others were with AMR-gene.

The primary hypothesis was to investigate any difference in the morphology and quantitative parameters obtained by the *QPM* images of four different bacteria. The

long-term aim was to examine if *QPM* can be used to image and classify bacteria. First, a systematic characterization of the *QPM* system is performed in terms of spatial phase sensitivity, temporal stability, spatial resolution, and defocus correction is done after phase recovery. Next, *QPM* imaging of four different bacteria sampled is done to investigate morphological parameter changes at a single wavelength. Further, the work is extended with multi-spectral *QPM* of these bacteria samples to develop new biomarkers related to them. In the future, the result can be fueled with the power of machine learning for the classification of these bacteria samples based on the quantitative parameters extracted from their *QPM* images.

List of Abbreviations

AMR	Antimicrobial resistance
Approx.	Approximately
AIA	Advanced iterative algorithm
CFU/ml	Colony-forming unit per mili liter
DIC	Differential interference contrast
DHM	Digital holographic microscopy
DPM	Diffraction phase microscopy
DPSS	Diode-Pumped Solid-State
E	Energy
En	Entropy
E. coli	Escherichia coli
ESBL	Extended-spectrum beta-lactamase
FOV	Field of view
FWHM	Full width half maximum
FTLS	Fourier transform light scattering
IACG	Interagency coordination group on antimicrobial resistance
K	kurtosis
LASER	Light amplification by stimulated emission of radiation
LB	Lysogeny broth
LED	Light-emitting diode
LOD	Limit of detection
MDR	Multidrug-resistant
MMFB	Multimode fiber
NA	Numerical aperture
OPD	The optical path length difference
PA	Projected area
PAV	Projected area to volume ratio
PBS	Phosphate buffered saline
PCM	Phase-contrast Microscopy
PCA	Principal component analysis
PFA	Paraformaldehyde
PTLS	Pseudo thermal light source
PLL	Poly(L-lysine)
PZT	Piezoelectric Transducer
QPM	Quantitative phase microscopy
QPI	Quantitative phase imaging

RD	Rotating diffuser
RI	Refractive index
RT	Room temperature
RCQS	Regional quality control system
K. pneumonia	Klebsiella pneumoniae
S. aureus	Staphylococcus aureus
SA	Surface area
SAV	Surface area to volume ratio
SC	Spatial coherence
Sk	Skewness
TC	Temporal coherence
UN	United nations
UNN	The University Hospital of North Norway
UiT	The Arctic University of Norway
WHO	World health organizations

Contents

List of Figures

List of Tables

Chapter 1

Introduction

The World Health Organization (*WHO*) has designated Antibiotic resistance (*AMR*) as one of the most severe global dangers to human health [2]. *AMR* occurs when pathogens no longer respond to the antimicrobial which they used to be in the past [2]. As a result of the rise of *AMR* pathogens, our potential to treat life-threatening infections is challenging. *AMR* pathogens are responsible for a considerable worldwide burden of disease and mortality. According to United Nations Ad hoc IACG (Interagency coordination group on antimicrobial resistance), 0.7 million people die annually due to some common infection that becomes resistant to antimicrobial [2]. Only in Europe, 33000 people die every year due to *AMR* pathogens [2]. According to a prediction made by Jim O'Neill in 2014 [5], if this number continues to grow in the same way, then by the end of 2050, around 10 million people will die due to *AMR* infections. Furthermore, this will cost the globe up to 100 trillion dollars and even exceed cancer related mortality, as shown in Fig.1.1 [5] [6]. Therefore, there is an urgent need to take the initiative to tackle this situation.

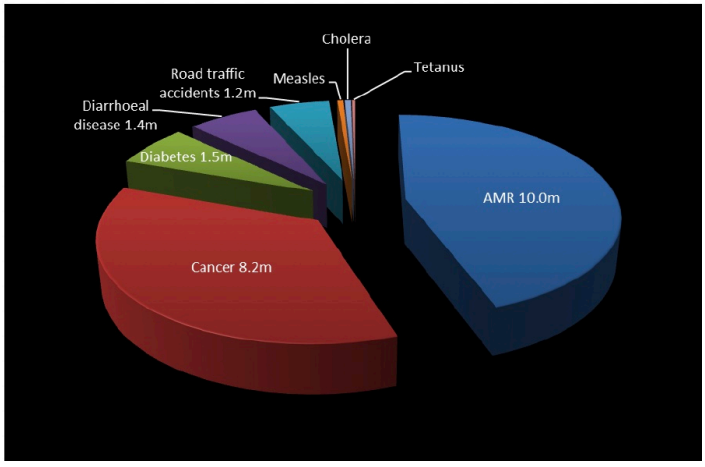

Figure 1.1: J
im O'Neill made the prediction (2014) [5] and further confirmed by Mara Baldry (2016) [6]. It reveals that the highest number of deaths will be due to antimicrobial resistance (*AMR*) if it grows in the same way. This number is even more significant than the fatality due to cancer [6].

The focus or scope of this thesis is as follows.

(1) Explore a microscopy technique also called quantitative phase microscopy (QPM) to identify different types of bacteria.
(2) Investigate the challenges associated with bacteria imaging using *QPM*, such as Brownian motion in bacteria, spatial phase sensitivity requirement, and defocus effect on the phase maps.
(3) Perform Quantitative phase imaging (*QPI*) of three different classes of the *AMR* and one type of *non-AMR* bacteria for their classification based on their morphological and statistical parameters.
(4) Dual-wavelength study of the *AMR* and *non-AMR* bacteria samples to determine spectral fingerprints if any.

This thesis covers imaging *AMR* and *non-AMR* bacteria cells using the *QPM* technique. Additionally, it provides a literature review of the field and identifies the associated challenges and limitations.

1.1 Choosing the suitable imaging modality

We needed to see through appropriate imaging techniques to differentiate bacteria. The optical microscopic imaging techniques to visualize bacteria cells can be broadly classified as:
(1) Labeling methods: fluorescence microscopy
(2) Label-free methods: phase-contrast microscopy (*PCM*), differential interference contrast (*DIC*) microscopy, darkfield optical microscopy, and *QPM*.

Using a bright field light microscope, the absence of contrast in images of nearly transparent specimens, such as bacteria cells, makes them difficult to image. This is due to insufficient amplitude fluctuations in the transmitted light through the sample.The contrast in imaging such specimens can be obtained by employing fluorescence microscopy techniques. However, it requires exogenous contrast agent to label different structures of the cells. Fluorescence microscopy allows researchers to investigate specific features in a bio-specimen with excellent specificity [7]. However, unfortunately, it is expensive and time-consuming. Also, labeling can alter the characteristics of bacteria cells; so label-free approaches seem to give the desired output. There are mainly three available imaging techniques. Other label-free methods, such as *PCM* and *DIC* microscopy, are not quantitative techniques, therefore, pose limitations for the identification of different bacteria samples if the difference between them is minute. On the contrary, *QPM* can quantitatively measure the differences between different types of bacteria cells.

1.2 Quantitative phase microscopy (*QPM*)

QPM is a non contact, non-invasive, and label-free approach that can precisely quantify a variety of parameters associated with biological specimens such as surface area, projected area, sphericity, volume, as well as statistical parameters(mean, variance, kurtosis, skewness). QPM has been implemented in various industrial and biological applications in the past [4][8]. *QPM* records images in the form of an interference pattern usually called an interferogram.

The interferograms contain both real and imaginary (complex) information about the specimen. The real part gives detail about amplitude, and the complex part provides phase information. The sample's complex information is encoded in a spatially modulated signal formed by interference or superposition of the sample and reference beam [4][8]. This encoded information is further numerically processed to acquire results in *QPM*.

1.2.1 The Basic principle of *QPM*

The basic principle of *QPM* gives details about the fact that how interference patterns have encoded phase information. When a plane wave illuminates a specimen under a microscope, the amplitude and phase of the transmitted light fluctuate due to the material's transmittance differences. At an image plane, the transmitted signal can be written as:

$$E(x,y,t) = |E_o(x,y)|.e^{-i(k.r-\omega.t+\phi(x,y))} \tag{1.1}$$

The detectors only record the intensity of light wave, which is the square of the modulus of the field $|E_o|^2$,

$$I = |E(x,y,t)|^2 = |E_o(x,y)|^2 \tag{1.2}$$

Thus, the phase information of the specimen is lost. However, the resulting intensity retains phase information if the image field interferes with another reference field *R(r)*, which is the basic principle of *QPM* [8].

$$R(x,y,t) = |R_o(x,y)|.e^{-i(k_r.r-\omega.t_r)} \tag{1.3}$$

The superposition of the reference beam and the sample beam forms an interference pattern. The total intensity due to the superposition of both fields at the image plane is as follows [8]:

$$I(x,y,t) = |E(x,y,t) + R(x,y,t)|^2 \tag{1.4}$$

$$I(x,y,t) = |E_o|^2 + |R_o|^2 + E^*(x,y,t).R(x,y,t) + E(x,y,t).R^*(x,y,t) \tag{1.5}$$

$$I(x,y,t) = |E_o|^2 + |R_o|^2 + 2|E_o||R_o|.Cos[(\omega.(t-t_r) - (k-k_r).r + \phi)] \tag{1.6}$$

It can be seen in Eq.1.6 that the resultant intensity has encoded phase information of the specimen and can be retrieved using phase recovery algorithms [8]. The phase recovery algorithms are discussed in *Chapter 2* of the thesis. The basic principle of *QPM* is based on the interference between the object and the reference beams. It is well known that light fields being superimposed must be coherent to form interference [13]. Here, the coherence properties of the light sources play an essential role to observe interference fringes in the *QPM* system.

Coherence

The sources which originate such waves of light that vibrate at a constant or fixed phase difference are known as coherent sources, and this property is called coherence. There are two types of coherence.
1) Temporal coherence [9]
2) Spatial coherence [9]

Temporal coherence

A constant or fixed phase relationship between light vibrations at two instants is called temporal coherence. Temporal coherence depends on the spectrum of the source [4][10][11]. The temporal coherence length l_c is the propagation distance over which a wave maintains a degree of coherence. A wave with a longer coherence length is closer to a perfect sinusoidal wave. The temporal coherence length l_c in mathematical form is written as follows [4]:

$$l_c = \frac{4ln2}{\pi}\frac{\lambda^2}{\Delta\lambda} \tag{1.7}$$

Eq.1.7 reveals that the greater the bandwidth $\Delta\lambda$, the shorter the temporal coherence length and vice versa. So, The temporal coherence length lc would be less for a broader spectrum.

Spatial coherence

Spatial coherence is associated with the size of the source of light. Spatial coherence describes the correlation of optical fields at two different spatial locations situated in the transverse direction of the beam propagation at the same moment [9][10][11][12].

1.2.2 Superposition of waves and Interference of light

The superposition of two coherent beams of light results in bright and dark fringes, and this phenomenon is called interference of light [13][14].

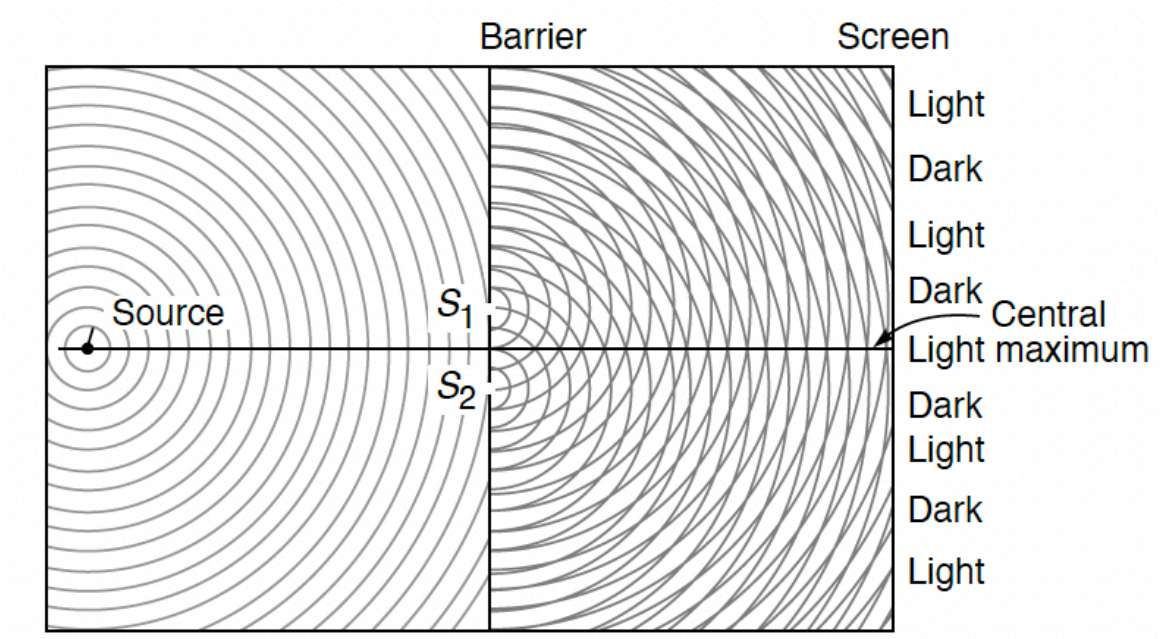

Figure 1.2: A single source of light is converted into two spatially coherent point sources, S_1 and S_2, by introducing a double slit in the path of the primary source of light: S_1 and S_2 separated by distance d. The size of the slit is small to make the light spatially coherent [13][14].

1.3 Methods to obtain two coherent sources

Coherence between light waves is the primary condition to obtain interference patterns. However, it is almost impossible for two independent light sources to be coherent. That is why a single source is usually converted into two light sources; this conversion can be accomplished in two ways. [13].

(1) Division of wave-front [13].

(2) Division of the amplitude of a single beam [13].

The instrument used to achieve interference is called an interferometer. Many interferometers work on either wave-front division or amplitude to obtain two coherent sources. The light from these coherent sources superimposes to produce an interference pattern.

1.3.1 Young's double-slit experiment

Young's double-slit experiment works on the principle of wavefront division and can be explained with the help of a Fig.1.4. A single source of light originates two spatially coherent point sources S_1 and S_2 by introducing a double slit (a small aperture) in the path of the primary source of light. These sources S_1 and S_2 are separated by distance d. A screen is held perpendicular to the point sources at a distance of L, as shown in Fig.1.4(a). The two beams reach on the screen and superimpose with each other to produce interference.

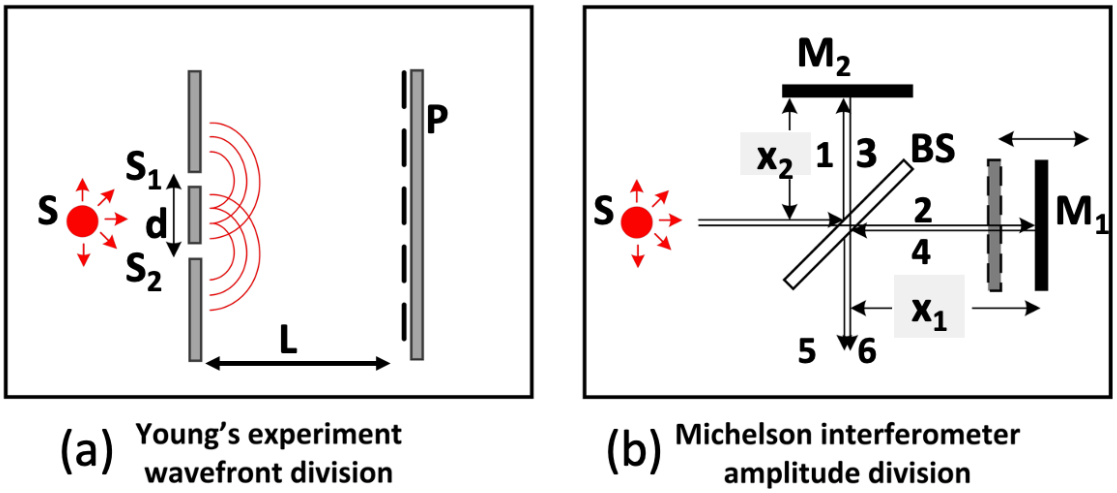

Figure 1.3: Methods to obtain two coherent sources from a single source of light are shown. In the left figure, a single source of light is transformed into two by the wave-front division with the help of double slits are placed in its path. This experiment is called young's double-slit experiment. In the right-side figure, a single source of light is transformed into two with the help of a beam splitter. The beam splitter divides the beam into two, and after reflection from two different mirrors, they recombine to produce an interference pattern. Such an interferometer is called a Michelson interferometer. [13].

The beam from the lower point source S_2 travels an extra distance of about $dsin\theta$ to reach the point, P. This extra distance is called path difference, which decides constructive or destructive interference condition at point *'P'* [13][14].

$$\delta = r_2 - r_1 = dsin\theta \tag{1.8}$$

Constructive interference

If the path difference is an integral multiple of the wavelength, then there will be a bright fringe on the screen [13][14].

$$\delta = dsin\theta = m\lambda \tag{1.9}$$

where $m = 0, \pm1, \pm2, ...$

Destructive interference

Alternatively, if the path difference is an odd integral multiple of the wavelength, there will be a bright fringe on the screen [13] [14].

$$\delta = dsin\theta = (m + \frac{1}{2})\lambda \tag{1.10}$$

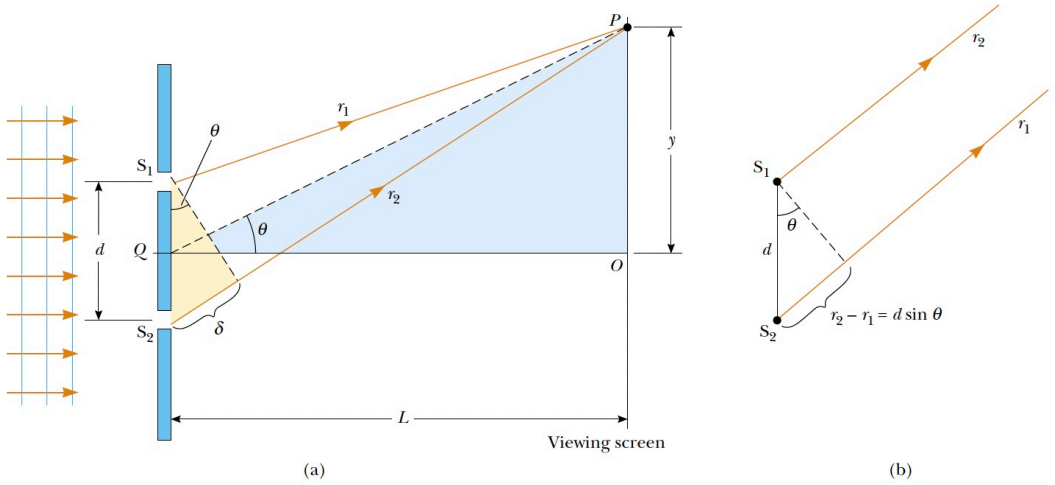

Figure 1.4: (a) Ray diagram of Young's double-slit experiment. Rays from a light source fall on the two slits separated by a distance d. *P* is a point; the screen is separated by a distance *L* from slits. (b) The two rays cover a distance r_1 and r_2 respectively to reach point *P*; they superimpose to produce interference. The path difference $\delta = r_2 - r_1$ decides if this interference will be constructive or destructive [13][14].

where $m = 0, \pm1, \pm2, ...$

1.3.2 Michelson interferometer

The Michelson interferometer works on the principle of division of amplitude and is depicted schematically in Fig. 1.3b, with *S* representing a light source and *BS* being a beam splitter [13]. M_1 and M_2 are high reflectivity plane mirrors. Mirror M_2 is static, while M_1 can be moved using translation stage [13]. Mirrors M_1 and M_2 are perpendicular to each other in the interferometer's typical setting, while the *BS* is at 45 degrees to the mirror [13].

Waves from source S are partially reflected and partially transmitted by the *BS*. The two resultant beams interact as follows: The reflected wave is reflected again at M_2, and this reflected wave is transmitted through the *BS* and is represented in Fig.1.3b as '5'. The transmitted wave is reflected by M_1 and reflected by the *BS*, resulting in the wave depicted as 6. Waves 5 and 6 superimpose with each other to produce an interference pattern.x_1, and x_2 are the distances of M_1 and M_2 from the plate *BS*. If the beam splitter is a glass plate, the beam reflected from mirror M_2 will undergo a phase change of π when reflected by the beam splitter. Since the extra path that one of the beams will traverse is 2x, where $x = x_1 = x_2$, the condition for destructive interference will be

$$2dcos\theta = m\lambda \tag{1.11}$$

Similarly, condition for constructive interference will be

$$2dcos\theta = (m + \frac{1}{2})\lambda \tag{1.12}$$

where m = 0, 1, 2, 3,... and $d = x_1 \sim x_2$ [13].

1.4 Optical configurations of *QPM*

All the optical configurations of *QPM* systems can be divided into two categories.
(1) Non-Common path *QPM*.
(2) Common path *QPM*.

1.4.1 Non-common path *QPM*

In the non-common path configuration of the *QPM*, the sample and reference beam do not follow the same path. One example is the Mach Zehnder[15] interferometer, as shown in Fig.1.5. In Mach Zehnder [15] interferometer using a beam splitter BS_1, a laser beam is split into a sample and reference beam. The sample and reference beam recombine at an angle to produce a high fringe intensity hologram at the *CCD* plane [4].

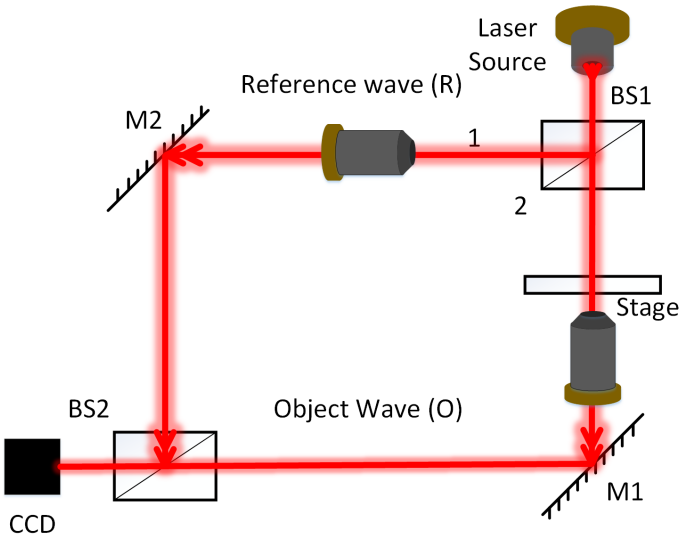

Figure 1.5: Schematic diagram of the transmission mode non-common path Mach Zehnder interferometeric. *MO* stands for microscopy objective, and *BS* stands for a beam splitter. *R* and *O* stand for reference and object wave [15].

Another example is Linnik[16][19-23] setup which is based on the Michelson interferometer and is discussed in *Section 1.3.1*.

1.4.2 Common path *QPM*

The interferometers with the same path for both the sample and the reference beams are common path interferometers [17].

An example is the common path diffraction phase microscopy (DPM), as shown in Fig.1.6 [17]. The sample and the reference beam follow the same path in this setup. The reference beam also contains the sample information. One can decode the sample information from the reference beam using the pinhole and diffraction grating. Grating is used to separate the reference and sample beam. The zero-order beam acts as a reference beam, and the first-order diffraction beam acts as a sample beam. The camera captures interference patterns of reference and sample beam [17].

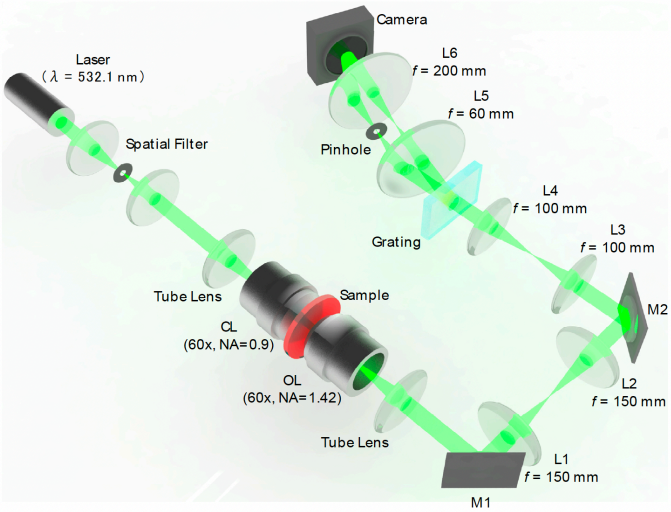

Figure 1.6: Diffraction phase microscopy experimental setup. A laser-interferometric microscope with a common-path geometry in the *DPM* configuration. Between the condenser and the objective lenses is a sample.*OL*stands for the objective lens, *CL* for condenser lens, *M1-2* for mirrors, and *L1-6* for lenses [17].

1.5 Geometrical vs. optical thickness

QPM measures the specimen's phase shift (rad or mrad) produced. Then this phase shift is used to find the *OPD* information. The geometrical and optical path length/thickness are related to each other. The *OPD* is the product of refractive index and geometrical thickness [24]. Let geometrical thickness is 't,' then.

$$OPD = \Delta n.t = (n_2 - n_1).t[24] \tag{1.13}$$

Despite the waves being in phase at the slits, the path difference δ introduces the phase difference ϕ between the waves at any point on the screen. The phase difference and path difference are related to each other as follows [14]:

$$OPD = \frac{\lambda}{2\pi}.\Delta\phi \tag{1.14}$$

In *QPM*, Eq.1.14 can convert the recovered phase information into *OPD*.

1.6 Phase sensitivity

We can characterize phase sensitivity in two.
1) Temporal phase sensitivity.
2) Spatial phase sensitivity.

1.6.1 Temporal Phase sensitivity

Michelson and Morley explicitly describe the difficulties involved in achieving the required phase stability in their interferometric experiments on the speed of light [8]: *"In the first experiment, one of the principal difficulties encountered was [...] its extreme sensitivity to vibration. This was so great that it was impossible to see the interference fringes except at brief intervals when working in the city, even at two o'clock in the morning" [8].*Temporal stability is arguably the most challenging aspect of establishing *QPI*. It gives information about the phase change observed at a particular point in the *FOV* as a function of time due to the system's instability. The issue that frequently arises while researching dynamic phenomena with QPI is: What is the smallest phase shift observed at a given point in the FOV? For example, examining red blood cell membrane fluctuations needs a displacement sensitivity of 1 nm, roughly equal to a temporal phase sensitivity of 5–10 mrad, depending on the wavelength [8]. Uncorrelated noise between two fields typically restricts the temporal phase sensitivity in time-resolved interferometric measurements. Hence the resultant signal

has a random phase in the cross-term [8].

$$I = \mid A \mid^2 + \mid B \mid^2 + 2 \mid A \mid\mid B \mid cos[\phi(t) + \delta\phi(t)] \tag{1.15}$$

Here, ϕ is the phase, and $\delta\phi$ is the phase noise. If $\delta\phi$ varies at random throughout the interval $(-\pi, \pi)$ during the time scales, the knowledge about the quantity of interest ϕ is lost. Experimenting with consecutive measurements of a stable sample/ without a sample is a quantitative approach to determine phase stability. The standard deviation is used to determine the temporal phase stability, $\delta\phi$, associated with a single point. This value specifies the minimum detectable phase value as a function of time [8].

1.6.2 Spatial Phase sensitivity

The spatial phase sensitivity of the system defines the minimum spatial phase variations due to either refractive index or height that the system can detect [8]. The standard deviation of a flat surface's reconstructed complete *FOV* phase image for spatial phase sensitivity measurement is determined. In contrast to temporal noise, there are no straightforward strategies to increase spatial sensitivity other than maintaining pristine optics and minimizing the coherence length of the illuminating light [8]. The spatial non-uniformities in the phase background are mostly caused by the random interference pattern (i.e., speckle) formed by fields scattered from impurities on optics, specular reflections from the system's different surfaces, and so on. This spatial noise is increased when high coherent sources, such as lasers are used [8]. Using white light significantly lowers the impacts of speckle while maintaining the need for a coherence area at least as broad as the field of vision [8].

1.7 Types of light sources used in *QPM*, their advantages and disadvantages

QPM system's spatial phase sensitivity is dependent on the light source type used to illuminate the specimens [9]. *QPM* uses the following light sources,

1. Halogen lamp (thermal light source): Halogen lamp has lower temporal and spatial coherence.

2. Light-emitting diodes *LEDs*: *LEDs* have partially low temporal and low spatial coherence.

3. Light amplification by stimulated emission of radiation (*Laser*): *Laser* has high temporal and spatial coherence.

4. Pseudo-thermal light source *(PTLS)* [9] A laser beam that has both high temporal and spatial coherence is sent through a revolving diffuser or a rough surface to produce the *PTLS*. The output of the diffuser provides a high temporal and partial spatial coherent light source. The spectral bandwidth and coherence length of different light sources generally used in

QPM are shown in Table. 1.1. The temporal coherence length of different light sources is shown in Fig. 1.7. Broadband light sources such as white and light-emitting diodes can

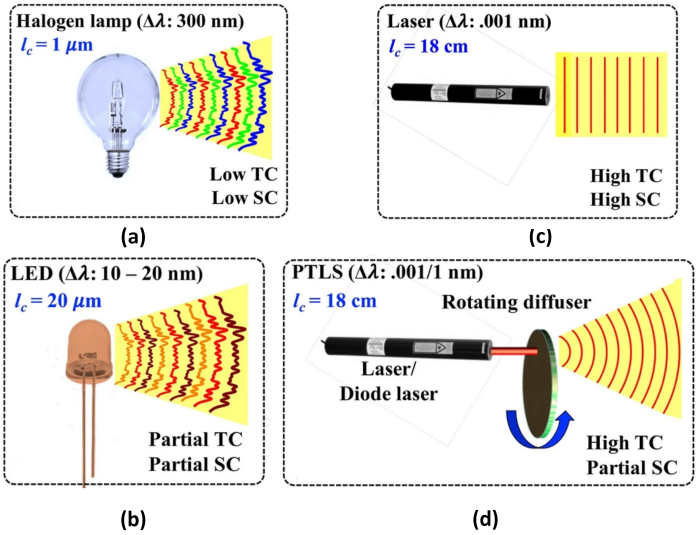

Figure 1.7: Schematic representation of light field illumination wave-front profiles in case of (a) halogen lamp,(b) *LED* (c) *laser*, and (d) *PTLS*, respectively. Coherence properties of different light sources, their coherence length, and bandwidth [25].

Table 1.1: Different light sources used in *QPM*, their bandwidth, and coherence length [9].

Light source	*Spectral bandwidth*	*Temporal coherence length*
Laser	0.001nm	18cm
Halogen lamp	300nm	1μm
LED	10-20nm	20 μm
PTLS	0.001/1nm	18cm

increase *QPM*'s spatial phase sensitivity [9]. However, the drawback to using such sources is either reduced temporal resolution or a smaller field of view *(FOV)*. On the other hand, these light sources have a higher phase sensitivity due to their shorter temporal coherence length. However, the interference occurs when the *OPD* between the object and the reference beam is within the light source's coherence length. As a result, producing an interference pattern with light sources of short temporal coherence length is challenging [9]. Furthermore, compared to narrow-band light sources like lasers, these light sources have relatively low photon degeneracy or the average number of photons per unit coherence volume [9].

The high photon degeneracy of lasers causes coherent and speckle noise in images, drastically reducing their quality. Hence, regarding photon degeneracy and coherent noise reduction, *PTLS* adoption in bright field optical microscopy outperformed traditional light sources (compared to lasers).

A high temporal and high spatial coherent light source is usually needed to acquire the interference pattern over the camera's entire *FOV* [9][16][25]. Unfortunately, the

image quality of a laser light source with high temporal and spatial coherence degrades because of coherent noise and parasitic fringe generation induced by various reflections from various surfaces of the optical elements [9][18]. The system's spatial phase sensitivity and measurement accuracy decreases as a result.

PTLS has lately piqued the curiosity of *QPM* researchers. *PTLS* offers the features of broadband and narrow-band sources, i.e., highly spatial phase sensitivity and interference across the whole *FOV* [9]. *PTLS* does not suffer from chromatic aberration of optical components or biological specimen dispersion problems. Having imaging speed restricted only by camera acquisition speed, *PTLS* can give single-shot phase imaging over broad *FOVs* without compromising spatial phase sensitivity or temporal resolution [9]. Furthermore, interference is achievable over a wider range of *OPD* between the object and the reference arm of the *QPM* system [9]. In this master's thesis, *PTLS* was used to image bacteria cells using *QPM*.

1.8 Fixation

The fixation method can retain the morphology of live cells after death, as they disintegrate fast if not fixed [26]. There are two types of fixation methods: additive and denaturing fixation. Additive fixation is the most popular in microscopy [26]. In this method, formaldehyde (CH_2O) is obtained from paraformaldehyde *(PFA)*, or formalin (since formaldehyde is a gas at room temperature) is used for fixation. It protects cell shape by cross-linking proteins through methylene bridges ($-CH_2-$), subsequently fixing cell shape [26]. Another method is the denaturing fixation method. This approach can denature proteins by lowering their solubility or breaking hydrophobic interactions, modifying protein structures, and inactivating enzymes. However, alcohols like methanol and ethanol can cause significant cell shrinkage if used solely in such methods [26]. Therefore, other denaturing compounds, such as acetone and acetic acid, are commonly used with alcohols to improve fixing efficacy [26]. In this master's thesis, the fixed samples were provided by a collaborator. However, the fixation of the samples was done by the first method, i.e., additive fixation. The protocol followed for the fixation is described in *Section 4.2*.

1.9 Background of bacteria imaging using *QPM*

QPM has developed as an essential tool for cell and tissue analysis. *QPI* functions on unlabeled specimens and is complementary to proven fluorescence microscopy, showing low photo-toxicity and no photo-bleaching. Moreover, *QPI* is gaining traction as a powerful, label-free image analysis method of thin tissues and cells [27].

Much work has been done in imaging cells and tissues using this technique. However, very few papers were published on imaging bacteria as it was difficult for bacterial imaging

due to lower contrast and noise. In the case of bacteria, the refractive index varies just in the second decimal from water (1.38 vs. 1.33 for water). Thus, for a one μm cell visualized at 405 nm, a standard phase change of around $\lambda/4$ or 45° might be challenging to overcome. However, the advantage of such tiny structures is that unwrapping is not necessary because phase changes are not more than 2λ [28]. A work published in 2018 demonstrated and verified a machine-learning identification technique based on linear logistic regressions that can detect the bacteria cells by *DHM* image reconstructions with an accuracy of over 90% and a localization error of about $7\mu m$. The identification was verified using two classes of microorganisms without labeling. The basis of this technique, and *MATLAB* implementation, was briefly explained [28].

In 2016 *Jay Nadeau* and his group found imaging bacteria cells challenging due to poor contrast, tiny cell size, and swift movement with high-speed direction changes. They used a combo of improved optical design and layout, customized chambers, and labeling with a non-toxic chemical to track bacterial test strains automatically. Based on *SNR* estimates, they discovered that etalon sample chambers outperformed other sample chamber designs substantially [24]. The anti-reflective *(AR)* coated etalons boosted the average *SNR* by 24% compared to the conventional microscopic examination. The combination of lower noise and higher *SNR* demonstrates the importance of excellent optical quality sample chambers in *3D* bacterial identification and tracking. For 488 nm illumination wavelengths, corrole or porphyrin dyes with high blue absorption were ideal. Other dyes may be used for more common wavelengths utilized in biological studies. According to them, it is unknown if these dyes are absorbent enough to be beneficial. They suggested that dye fluorescence is unnecessary for this use, and in the future, one can investigate colorimetric agents that absorb but do not fluoresce [24]. In Fig.1.8, the phase reconstruction has shown with and without dye. The images were taken at best focus and about 6μm off from best focus [24].

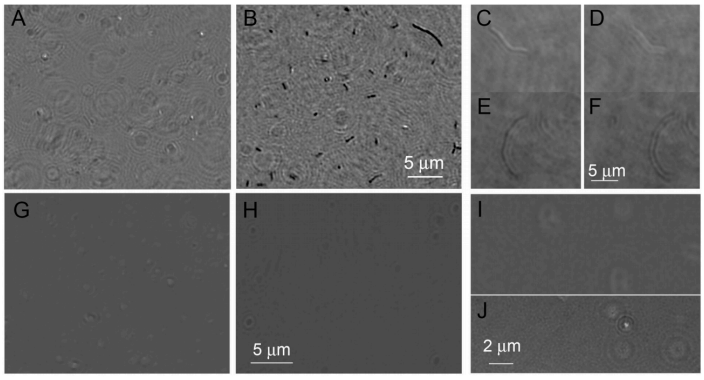

Figure 1.8: Reconstructions of a single plane phase of bacterial cultures with and without corrole dye. (A) *E. coli* is unlabelled. (B) *E. coli* with labeling. (C) *B. subtilis* unlabelled at apparent best focus. (D) *B. subtilis* unlabelled 6 μm from best focus. (E) *B. subtilis* labeled at apparent best foc s. (E) *B. subtilis* labelled 6 μm from best focus. (G) *V. alginolyticus* unlabelled. (H) *V. alginolyticus* label d. (I) Zoom view of *V. alginolyticus* unlabelled. (J) Zoom view of *V. alginolyticus* labeled [24].

In 2016, scientists devised and experimentally proved a simple but powerful laser approach for measuring bacterial activity in food by studying laser speckle decorrelation using *QPM*. Several experimental validations demonstrated that spontaneous bacterial activity induces substantial decorrelation in laser speckle dynamics. Although the current approach can detect bacterial activity, it cannot distinguish between various harmful bacterial strains. Nonetheless, the present technology can be employed in multiple applications where the identification of bacterial activity is more critical, such as avoiding food toxicity or performing prescreening tests. Furthermore, the proposed approach may be used in research applications involving the measurement of the bacterial activity or the efficiency of antibacterial medications [29].

DHM could attain spatial resolution several times smaller than a bacterial cell using Mach Zehnder devices and high numerical aperture *(NA)* microscope targets in the blue wavelength range. *DHM* is a very effective tool for visualizing bacterial motion in three dimensions, and it will become increasingly valuable as contrast methods improve. However, the employment of dyes to boost the quantitative phase's amplitude and contrast is still in its early stages [30].

In 2020 in a publication, a fast, label-free, and economical biosensor was designed for the detection of *E. coli* has a 2.2 CFU / ml limit of detection *(LO)*. Compared to bacterial molecular components detection techniques, their framework focuses on the direct binding of individual bacteria to the sensor via antibody-antigen coupling, which has the benefit of requiring minimal sample pre-processing [31]. Furthermore, they claimed that the suggested biosensor's large *FOV* and real-time detection capacity allowed them to monitor bacteria size development. Furthermore, recognizing and counting colony-forming units *(CFU)* is considerably faster than it takes for colony units to be visible to the human eye [31].

In 2015, a research publication presented and experimentally proved an optical approach based on Fourier transform light scattering measures and statistical categorization to accomplish quick and label-free detection of bacteria [32]. The *FTLS* approach produces 2D angle-resolved light scattering maps for single bacteria(rod-shaped). These maps are then carefully studied, and the specific fingerprint for each bacteria is determined using statistical categorization [32]. Thus, a single light scattering measurement may categorize a new undiscovered bacteria. In addition, bacteria produce nanometric extracellular membrane vesicles involved in many biomedical applications [32]. To assess the uniqueness of membrane vesicles derived from bacteria cultures, phase imaging and atomic force microscopy were used to examine membrane vesicles. Phase imaging may be used to characterize the physical characteristics of particular membrane vesicles in an individual membrane vesicle population with a wide range of vesicle sizes ranging from twenty to one hundred and fifty nanometers [32]. Furthermore, a method was devised for comparing the physical features of membrane vesicles between samples quantitatively. This enabled a study of the physical characteristics of membrane vesicles gathered from different bacterial

species [32].

In 2017, a paper was published. The authors demonstrated the categorization of healthy and malignant cells using *QPM*. They compared healthy cells to tumor and metastatic cancer cells, using tumor samples and normal tissues from the same people [33]. The *OPD* maps of the cells were recovered after acquisition and utilized to generate 15 parameters derived from the cellular 3D shape and texture [33]. We discovered vital statistical significance in the difference between the groups in most of the parameters estimated after evaluating tens of cells in each group, with the same patterns for all statistically significant parameters [33]. Furthermore, a specifically developed machine learning algorithm based on the phase map derived characteristics correctly categorized the cell type (healthy/cancer/metastatic) with 81–93% sensitivity and 81–99% specificity [33]. They suggested that the *QPI* strategy for liquid samples described in this study might serve as the foundation for enhanced approaches for staging freshly isolated live cancer cells in imaging flow cytometers [33].

Chapter 2

Phase recovery methods and Focus correction algorithm

This section covers the mathematical forms of all the algorithms used in this thesis. My supervisor Azeem Ahmed provided these algorithms, and I made them compatible with my master's thesis using MATLAB.

The phase information is stored in the recorded interferogram in *QPM*, as detailed in *Chapter 1*, *Section 1.2.1*. Therefore, the next important step is to extract this phase information from the interference pattern acquired experimentally. There are many methods for phase recovery. Mainly we can categorize phase recovery methods in two.
(1) Single shot(frame) method
(2) Multi shot(frames) method

2.1 Fourier transform method

Fourier transform is a single-shot technique. It can recover phase information about a sample from a single interferogram, decreasing acquisition time. There is a trade-off between phase change inaccuracy and acquisition time [4][23]. Eq.1.6 is rewritten as a 2D single interferogram with high-density fringes with a frequency of v_0.

$$I(x,y) = E(x,y) + R(x,y).Cos(2\pi v_0 x + \phi(x,y)) \tag{2.1}$$

Here I(x,y) is the 2D recorded intensity of interferogram in x and y-coordinates The desired information is in phase $\phi(x,y)$, and E(x,y) and R(x,y) represent undesirable irradiance variations caused by non-uniform light reflection or transmission by a test sample. Since,

$$cosx = \frac{e^{ix} + e^{-ix}}{2} \tag{2.2}$$

Using Eq.2.2, one can rewrite the intensity of the input fringe pattern as follows [34].

$$I(x,y) = E(x,y) + R(x,y)\frac{e^{i2\pi v_0 x+\phi} + e^{-i(2\pi v_0 x+\phi)}}{2} \tag{2.3}$$

Introducing a new variable

$$W(x,y) = 1/2R(x,y).e^{i\phi} \tag{2.4}$$

Putting values from Eq.2.4 in Eq.2.3.

$$I(x,y) = E(x,y) + W(x,y)e^{2\pi i v_0 x} + W^*.e^{-2\pi i v_0 x} \tag{2.5}$$

Using a fast fourier transform (FFT), resulting in Eq. 2.6 [34].

$$H(v,y) = e(v,y) + w(v-v_0,y) + w^*(v+v_0,y) \tag{2.6}$$

$e(v,y)$ is a background *(DC)* term at the Fourier plane's origin. The term $w(v-v_0,y)$ is a plus 1 order term that includes details about the object and is located at (v,v_0). Similarly, $w^*(v+v_0,y)$ is a minus 1 order term at $(-v,-v_0)$ that contains complex conjugate details about the specimen. Eq. 2.6 can be reduced to the following form after filtering out zero-order and minus one order terms [34]:

$$H(v,y) = w(v-v_0,y) \tag{2.7}$$

The filtered spectrum is transferred at the origin or center, and then inverse Fourier transform is used to obtain the complex signal(W(r)) and then phase information [34].

$$\phi(x,y) = tan^{-1}(\frac{Im(W(x,y))}{Re(W(x,y))} \tag{2.8}$$

The recovered phase map is in wrapped form, and its values are between $-\pi$ and π. So phase unwrapping is made using a minimum $L_P - norm$ two-dimensional (2D) phase unwrapping algorithm [4]. The Fourier transform approach is a single shot phase recovery algorithm that allows high imaging. However, the zero and first-order peaks in the Fourier domain must be well separated for a lossless reconstruction of the object, which necessitates a high density of fringes [23]. In my thesis, I used this method to find the spatial and temporal sensitivity of the system used for imaging.

2.2 Multishot phase reconstruction algorithms/methods

There are many multishot phase reconstruction algorithms, i.e., Five frame phase-shifting algorithm and PCA.

2.2.1 The Five frame phase-shifting algorithm

The Five frame phase-shifting algorithm is highly famous over other phase-shifting algorithms due to its reasonable phase error and acquisition time. However, there is a trade-off between phase error and acquisition time. For example, if we attempt to reduce the phase change error by adding more frames (say N), the acquisition time also adds up, or vice versa [4][35][36]. Hariharan [37] developed a phase-shifting algorithm using five frames for phase recovery with a reasonable phase error value. One can write the intensity of five phase-shifting two-dimensional interferograms at a specific wavelength [35].

$$I_1(x,y) = U(x,y) + R(x,y) + 2\sqrt{U(x,y).R(x,y)}cos(\phi(x,y) - 2\delta) \tag{2.9}$$

$$I_2(x,y) = U(x,y) + R(x,y) + 2\sqrt{U(x,y).R(x,y)}cos(\phi(x,y) - \delta) \tag{2.10}$$

$$I_3(x,y) = U(x,y) + R(x,y) + 2\sqrt{U(x,y).R(x,y)}cos(\phi(x,y)) \tag{2.11}$$

$$I_4(x,y) = U(x,y) + R(x,y) + 2\sqrt{U(x,y).R(x,y)}cos(\phi(x,y) + \delta) \tag{2.12}$$

$$I_5(x,y) = U(x,y) + R(x,y) + 2\sqrt{U(x,y).R(x,y)}cos(\phi(x,y) + 2\delta) \tag{2.13}$$

Here U(x,y) and R(x,y) represents the intensities of sample and reference beams. $\phi(x,y)$ is the phase changes associated with the sample. Also, The following expression can determine the phase knowledge $\phi(x,y)$ relative to the test object [35].

$$\phi(x,y) = \tan^{-1} sin\delta \frac{2(I_4(x,y) - I_2(x,y))}{I_1(x,y) - 2I_3(x,y) + I_5(x,y)} \tag{2.14}$$

The main limitation of five frame phase-shifting algorithm is that one can not implement it on unequal phase shifts [37]. Phase-shifting interferometry requires equal multi-phase shifted interferograms for the phase recovery. However, traditional phase-shifting algorithms can not be implemented with unequal phase-shifted interferograms as they generate fringe-like modulation error in the phase reconstruction [37].

2.2.2 Principal component analysis *(PCA)* algorithm

The principal component analysis *(PCA)* can extract phase information from randomly phase-shifted interferograms. Moreover, it is rapid and easy to use as well [38]. For example, one can write a set of 2D interferograms as follows:

$$I_n(x,y) = E(x,y) + R(x,y)Cos[\phi(x,y) + \delta_n] \tag{2.15}$$

'E' denotes the background illumination, 'R' represents the modulation, and ϕ is the phase.δ denotes the phase steps. The Eq.2.15 can be expanded and written as follows.

$$I_n(x,y) = E(x,y) + R(x,y)[Cos\phi Cos\delta_n - Sin\phi Sin\delta_n] \tag{2.16}$$

Introducing four new variables γ_n,ζ_n,I_1 and I_2 to put in Eq. 2.16 are as follows:

$$\gamma_n = cos\delta_n \tag{2.17}$$

$$\zeta_n = sin\delta_n \tag{2.18}$$

$$I_1 = R(x,y).Cos\phi \tag{2.19}$$

$$I_2 = R(x,y).Sin\phi \tag{2.20}$$

Finally, Eq.2.16 is simplified as follows:

$$I_n = \gamma_n I_1 + \zeta_n I_2 \tag{2.21}$$

One can decompose any interferogram (without background term)into two uncorrelated quadrature signals I_1 and I_2, which roughly prove the following statement [38].

$$\sum_{x=1}^{+N_x}\sum_{y=1}^{+N_y} I_1(x,y)I_2(x,y) \equiv 0 \tag{2.22}$$

PCA is a statistical strategy for shrinking the size of an image or data set. It consists of a mathematical procedure that reduces potentially associated images into the minimum number of uncorrelated images(principal components) [38]. The principal components are obtained by linearly combining the primary variables that indicate the ideal subspace of a given dimension in a least-square sense [38]. *PCA* is mainly composed of three parts. Presume there are n images of $(n_x n_y)$ and they represent as a matrix as

$$x = [x_1 + x_2 + x_3 + ... + x_n]^T \tag{2.23}$$

The covariance matrix C_m from x is calculated first in the PCA technique.

$$C_m = (x - \mu_x)(x - \mu_x)^T \tag{2.24}$$

Each element in every column of μ_x corresponds to the average value of the corresponding column of x. Since C_m is a real and symmetric matrix, one can obtain real eigenvalues and orthonormal eigenvectors. Therefore, matrix theory can diagonalize the covariance matrix C_m. The second part of the *PCA* approach is the diagonalization procedure using the singular

value decomposition algorithm.

$$D_m = ACA^T \tag{2.25}$$

Here

D_m =diagonal matrix

A = transformation matrix. The third step uses the Hotelling transform to obtain the principal components.

$$y = A(x - \mu_x) \tag{2.26}$$

The eigenvalues of the first two main components are the highest and correspond to the $I_1$and I_2 signals. Since we randomly assign the cosine and sine signals to the first and the second primary component, the technique, cannot determine the proper global phase sign. The phase ϕ is as follows:

$$\phi = arctan\frac{I_2}{I_1} \tag{2.27}$$

PCA technique is relatively fast and straightforward to implement; therefore, it is not time-consuming. The approach does not require foreknowledge of the phase steps or conditions for the background and modulation terms. *PCA* is possible to implement on unequal phase shifts [38]. In short, we need to make a compromise between time and accuracy in *PCA* compared to another random phase-shifting algorithm such as the Advanced iterative algorithm *(AIA)* for phase recovery [39]. *AIA* [49] takes more time for phase recovery but gives artifacts free output than *PCA* [38] takes less time to extract phase information but can not remove artifacts that well. In my thesis, I used this method to extract phase information of all the recorded interferograms of bacteria samples.

2.3 Defocus correction algorithm

For accurate measurements of phase and subsequently phase-related morphological parameters focus correction is significant. Its first step is to obtain angular spectrum by employing the Fourier transform of the complex signal E(x, y; 0). Here we suppose that the signal is propagating along the z-axis, i.e., z=0 [19].

$$A(v, w; 0) = \int^{+\alpha} \int_{-\alpha} E(x, y; 0) \exp(-2\pi j(vx + wy), dx\, dy \tag{2.28}$$

This Eq.2.28, v, and w are the transform variables concerning λ. Then, The field is propagated to various planes using angular spectrum [19].

$$A(v, w; z) = A(v, w; 0)T(v, w) \tag{2.29}$$

Where

$$T(v,w) = \begin{cases} e^{-j\frac{2\pi z}{\lambda}\sqrt{1-(\lambda v)^2-\lambda w^2}}, & \sqrt{v^2+w^2} < \frac{1}{\lambda}, \\ \\ 0, & otherwise \end{cases} \tag{2.30}$$

T(v,w) is called free-space transfer function. The next step is to calculate the inverse Fourier transform to acquire a complex field in the spatial domain [19].

$$E(x,y;z) = \int^{\alpha}\int_{-\alpha} A(v,w;z)e^{j2\pi(vx+wy)} \quad dv\ dw \tag{2.31}$$

The complex field 'E(x,y;0)' is produced from the phase-shifting methods, as in our case, the Fourier transform approach. To compute the defocus distance, one can propagate the field in various planes ranging from – r to +r (in μm). The amplitude variance associated with each complex field E is determined from the following equation [19].

$$\sigma_a^2 = \frac{1}{\mu}\sum\sum[|E(v,u;z)| - \mu]^2 \tag{2.32}$$

Where μ is the average of the complex field's amplitude at distance r, plotting the amplitude variance σ_a^2 as a function of distance r yields the sharpness curve. The objective lens's defocus length or a minimum of the sharpness curves determines the objective lens's rear focal plane.[19] The complex field ′E(x, y; 0)′ is propagated by the determined defocus length to generate the samples' phase map [19]. I used this method to correct the amount of defocus in the images.

Chapter 3

Challenges during the project proposed solutions

3.1 Mobility of bacteria and adopted sample preparation protocol

The main challenge in bacteria imaging is mobility due to their Brownian motion, which is high when the size of structures is negligible. We first attempted to make a 1mm agarose slide, pipette 3 to 10 μl cell suspension, and shield it by the cover glass(agarose layer was under the sample); this method was not successful as the thickness of Agarose was not uniform, which caused an aberration in the interferogram. Next, we tried antifade mounting reagents on a slide, but it could not immobilize the bacteria. Further, we tried 0.1% poly-L-lysine *(PLL)* coating on sample substrate (silicon wafer in our case) and found it suitable to reduce the mobility of bacteria. First, the sample substrate is incubated for 10-15 minutes for *PLL* coating. The *PLL* is then removed and rinsed with water to make its thin coating on the substrate. The bacteria sample is then pipetted on top of the region, incubated with *PLL*, and allowed to settle down for 10-15 minutes.

3.2 Different *QPM* configurations and their pros and cons in terms of resolution

Initially, we observed the sample inside a petri dish using a PDMS chamber and cover glass on top of the specimen using Mach-Zehnder interferometer-based transmission mode *QPM*. Due to the horizontal reference arm objective lens, we could not use a high *NA* objective lens like water immersion 60x/1.2 *NA* objective lens as immersion media in the reference arm could make the interferometer unstable.

We used a Linnik interferometer (Reflection mode *QPM*) with a 60X1.2 *NA* water immersion objective lens to not sacrifice the resolution. The details about this setup are in the next chapter.

3.3 Low vs. high temporal coherent light source

First, *PTLS* generated from four different wavelength laser diodes (at 450 nm, 520 nm, 638 nm, 808 nm) are utilized for multispectral *QPM* of bacteria samples. Due to their low temporal coherence length, these light sources increase the spatial phase sensitivity of the system compared to high temporal coherent lasers.[9] However, these light sources' low temporal coherence length requires the *OPD* adjustment between the object and the reference arm of *QPM* to generate high contrast interference fringes.[9] This leads to the formation of circular fringes using non-identical objective lenses in the *QPM* system. [9] We observed that circular fringes have spatially varying frequency of the interferogram over the *FOV*, which leads to the generation of ringing artifacts in the recovered phase images using phase-shifting algorithms. Therefore, high temporal coherent light sources are used, which helped us obtain straight fringes and artifacts free phase reconstruction as illustrated in Fig. 3.1b. Unfortunately, we could not perform experiments at other wavelengths due to the unavailability of high temporal coherent lasers at blue and *IR* wavelengths regimes. We expected the projected area to remain the same when imaged through different wavelengths. Instead, it was changing with the change in wavelength. These results might be due to defocus in images, as focus correction is significant in quantitative phase images. Wrong-focused images can lead to wrong conclusions. It was possible to correct the defocus mathematically, but it required data free of ringing artifact.

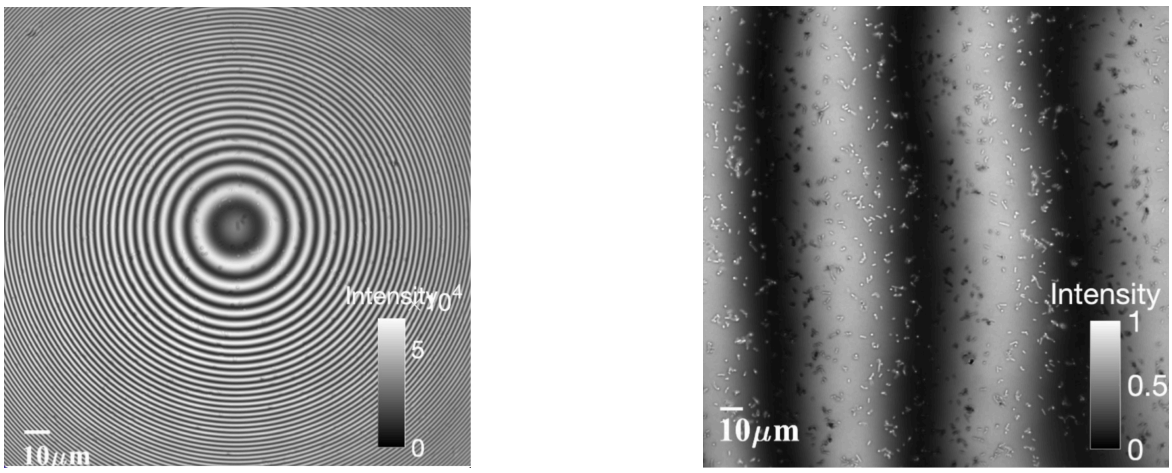

(a) (b)

Figure 3.1: An illustration of the output of two types of lasers(Diode with high-density circular fringes and low coherence length and *DPSS* with low-density circular fringes and high coherence length) along with rotating diffuser to make them PTLS. A comparison between recorded interferogram(a)low l_c light source with circular high-density fringes obtained at zero *OPD*(b)high l_c light source with straight fringes of low density (b)Comparison between reconstructed phase images using (a)Low l_c light sources with ringing artifact zoomed-in (b)high l_c light source without any ringing artifact.

In Fig.3.1a, an illustration of comparison of interferogram obtained when imaged using

low coherence length light with circular fringes and *DPSS* laser with high coherence length and straight fringes.

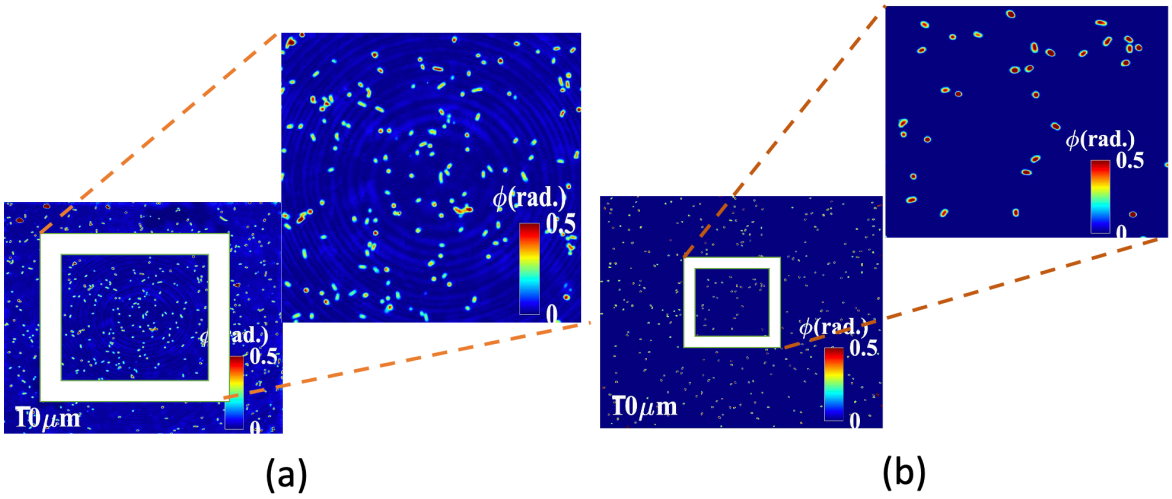

Figure 3.2: An illustration of the output of two types of lasers(Diode with high-density circular fringes and low coherence length and *DPSS* with low-density circular fringes and high coherence length) along with rotating diffuser to make them PTLS.Comparison between reconstructed phase images using (a)Low l_c light sources with ringing artifact zoomed-in (b)high l_c light source without any ringing artifact.

Fig.3.2a, the ringing artifact is zoomed in to make a clear vision in Fig.3.2b shows the reconstructed phase image obtained using *DPSS* laser without any ringing artifact.

3.4 Effect of defocus on the phase recovery

The reconstructed phase map has a different amount of defocus at other regions; therefore, it is necessary to do piece-wise focus correction for accurate phase map reconstruction. For this, we adopted two different approaches; (1) split the full *FOV* image into multiple sub-images and then apply focus correction algorithm, (2) focus correction at a single bacteria level. First, we cropped the recovered phase map in 16 sub-images, i.e., 4X4 matrices, and made a stack of these sub-images as shown in Fig.3.3. Thus, each cropped image had 576x576 pixels. Then, we calculated the defocus amount separately in all 16 parts. This approach, however, was not highly precise because the magnitude of defocus varied even within the sub-images. Therefore, the defocus correction is done at a single bacteria level for the most accurate quantification of the phase maps, as shown in Fig.3.4 After converting the reconstructed phase map into a stack of cells, defocus correction for individual bacterium cells is performed. This procedure was successful since individual bacteria cells were defocus corrected, and all focus bacteria cells were used for further investigation. Here in Fig. 3.4c, it is visible that bacteria cells are getting focused. Some of

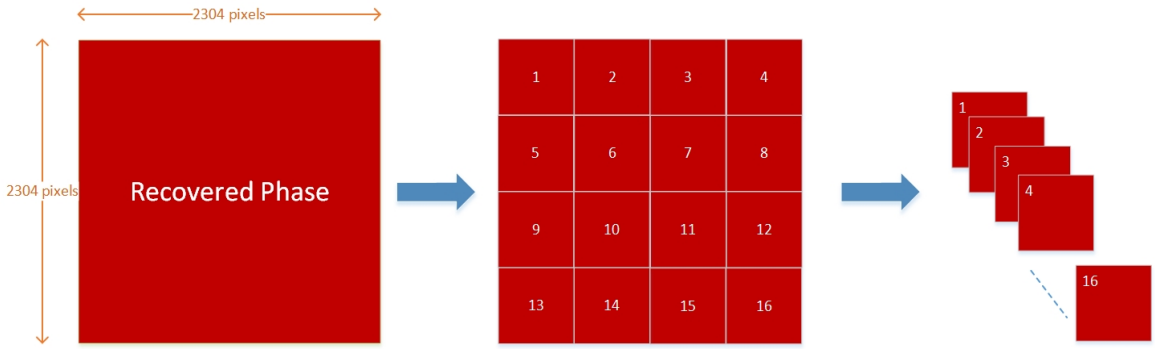

Figure 3.3: (a)Schematic representation of recovered phase map cropped in 16 parts(b) illustrates a stack of respective cropped parts.

the bacteria cells are removed from the image through segmentation; we wanted to have a single bacteria cell in an image to have accurate quantitative analysis. .

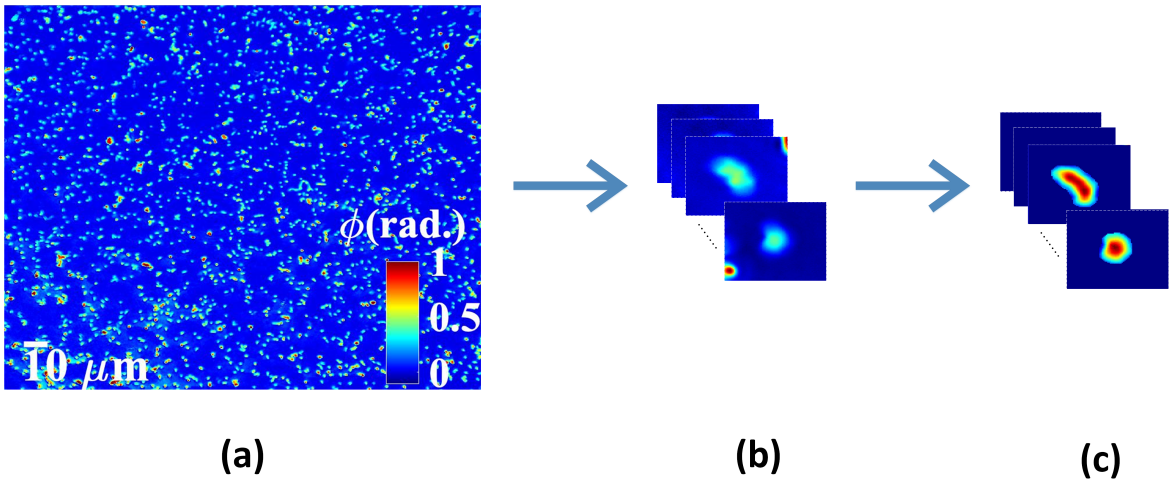

Figure 3.4: An illustration of converting a phase image into the single-cell level and its defocus correction (a) representation of recovered phase map and (b) illustrates a stack of single cells (c) defocus correction and segmentation on the single-cell stack.

3.5 Sample concentration

Sample concentration was not uniform in all samples. Therefore optimization of the concentration is done so that the cells are neither too sparse nor too dense in the *FOV*. Moreover, to have a desirable concentration, bacteria samples are left for 30 minutes so that all bacteria cells present in the sample volume settle on the substrate. Moreover, this is necessary to determine the sample's actual concentration. Otherwise, when all the bacteria floating in the sample container settle later during imaging, the sample concentration would rise.

3.6 Sensitivity of set up

The main challenge was that the system was susceptible to even slight movement and vibrations that were the cause of noise in the images. Therefore, the experiments are conducted carefully on a vibration isolated optical table.

Chapter 4

Material and methods

4.1 Selection of bacteria samples and their origin

We imaged four bacteria samples, out of which three of them were of the *AMR* gene, and one was with the *non-AMR* gene. We took the same bacteria class *(E. coli)* in both types of genes. *E. coli-1* was of *non-AMR* gene, and *E. coli-2* was of *AMR*. *Table 4.1* gives some information about the bacteria species taken for imaging.

4.1.1 Escherichia coli-1 *(E. coli-1)*

The origin of *E. coli* strain *CCUG17620* is the Culture Collection University of Gothenburg, Sweden. Its source is human. Its variance is O6: KN and tested by the Regional quality control system *(RCQS)* for international control for sensitivity testing [40][41].

4.1.2 Escherichia coli-2 *(E. coli-2)*

The origin of *E.coli* strain *NCTC13441* was culture collection at Public Health England. It was cultured on the nutrient agar at 37°C for 24 hours under aerobic conditions. Its antigenic property is O25:H4 (which is capsule and flagella antigen) [42][41]. It produced CTX-M-15 ESBL.

4.1.3 Klebsiella pneumonia *(K. pneumonia)*

The Norwegian National Advisory Unit provided *K. pneumonia* strain *A2-23 (blaCTX-M-gr.1)* on Detection of Antimicrobial Resistance (K-Res), University Hospital of North Norway, Tromsø. Klebsiella belongs to the class of bacteria called Enterobacterales, can become resistant to carbapenems, and *K. pneumonia*, in particular, has recently become resistant to this class of antibiotics. *K. pneumonia* is bacteria that have developed *AMR*, most recently to the class of antibiotics known as *carbapenems*. *Carbapenems* are usually used against multidrug-resistant *(MDR)* bacterial infections [41].

Table 4.1: Overview of all the bacteria samples, their size, shape and *AMR*-gene [41].

S.no	Bacteria name	Gram stain	Shape	Size	*AMR* gene
1	*E. coli*(CCUG17620)	Negative	Rod	1-2µm by 0.5µm	—
2	*E. coli*(NCTC13441)	Negative	Rod	1-2µm by 0.5µm	CTX-M-15
3	*K. pneumonia*(A2-23)	Negative	Rod	2µm by 0.5µm	CTX-M-1
4	*K. pneumonia*(CCUG35600)	Positive	Spherical	0.5µm by 0.5µm	mecA

4.1.4 Staphylococcus aureus *(S. aureus)*

S. aureus strain *CCUG35600* was obtained from Culture Collection University of Gothenburg, Sweden. It is obtained by culturing on blood agar at 37°C under anaerobic conditions and tested by the regional quality control system *(RCQS)*. It is resistant to many antibiotics but sensitive against gentamicin [41][43]. All samples were collected and fixed in Hamar by a collaborator and sent to us for the experiment's performance at the same time point.

4.2 Culture and fixation of bacterial cells

The culture and fixation of the bacteria cells were done by a collaborator and then were sent to us. Their group adopted the following steps:
1) The bacteria cells were directly incubated from frozen (-80 °C) to 3 ml liquid Lysogeny broth *(LB)* media and used cultures after 20 hours of incubation at 37 °C.
2) Each sample was centrifuged, and 2 ml of media was removed and resuspended in the remaining media. After collecting the cells for concentrating them, the cells were resuspended in *PBS* to reduce the presence of *LB* components within the samples.
3) Next, in 1 mL of *PBS*, the pellets were suspended. Then, 900 μl suspension was mixed with 900 μl 4% *PFA* (pH 7.15).
4) For 1 hour, the suspension was incubated at room temperature.
5) Next, it was centrifuged and washed with 1.5 ml *PBS* and the second wash with 1 ml *PBS* (per tube). At last, the centrifuge resuspended each pellet in 500 μl *PBS* and transferred the solution to a smaller tube for shipping.

4.3 Sample preparation

First, we diluted them using phosphate-buffered saline *(PBS)* in 3:50 (30 μl sample in 500μl, *PBS*). Next, we used a *PDMS* chamber on a silicon wafer and pipetted 0.1% poly-L-lysine *(PLL)* of about 10μl inside the chamber. We let *PLL* in the *PDMS* chamber for 10 to 15 minutes, then pipetted it out of the *PDMS* chamber. Finally, bacteria cells were placed on a reflective silicon substrate in a *PDMS* chamber and covered with an 18mm coverslip for

QPM measurements.

4.4 Experimental setup

The upright *QPM* with Linnik interferometric microscope, was used to capture the images of fixed bacteria samples. A Linnik interferometer[19][20][21][22][23] is a two-beam interferometer used in microscopy. The basic setup is the same as an interferometer designed by Michelson [15].

We used a laser with a maximum power of 500 mW or *PTLS* generation. The power efficiency was kept to be approximately equal to 10%. The intensity at the sample is measured to be equal to 10 nW/μm^2 at 532nm and 660nm wavelengths. To break the spatial coherence of the light from a continuous laser source, we used a revolving diffuser. We projected the laser beam at a distance of around 40 mm from the diffuser's center. The diffuser's speed is kept at 240 revolutions per minute *(RPM)* to allow adequate speckle-noise averaging within the camera's exposure time (30 ms). The rotating diffuser created a temporally changing speckle field, which resulted in a considerable reduction in speckle contrast [9][16] [20][21][25][33]. We coupled the diffuser's output into a multimode fiber bundle *(MMFB)* positioned at about one millimeter from the diffuser using a lens L_1.

The output of the *MMFB* is collimated using the lens L_2, which has a focal length of 75 mm. And then, the beam is focussed onto the rear focal planes of the objectives MO_2 (10x/0.25) and MO_3(60x/1.2) using lens L_3 having a focal length of 125 mm and a beam splitter. The beam splitter divides the input beam into two. It directs one to the reference mirror and the other to the sample mirror. MO_2 andMO_3 project collimated light to the sample and reference mirrors. The object and the reference mirror reflect light. These beams are collected once more by the objective lenses MO_2 and MO_3 and recombined at the Beam splitter. Lens L_4 of focal Length of 200 mm collects the object and reference waves, which interfere to produce interference patterns. The interferograms were captured using an *ORCA-Fusion (DIGITAL CAMERA C14440)* and shown on a computer screen *(Philips 240B4QPYEB/00)*. A piezoelectric transducer *(PZT)* is used to generate a phase shift between the sample and reference arms. First, light through the reference arm is blocked, and the sample is focused. Then, light is allowed through the reference arm and observed the interferogram's contrast on the screen. A good interferogram contrast always reflects that the sample is the best focus in the correct plane. Finally, we recorded an interferogram of the sample with an image sensor. We imaged fixed bacteria; only wavelength changes, keeping all other factors constant. Since the refractive index is a function of wavelength, so, we can probe the properties which are wavelength dependent.

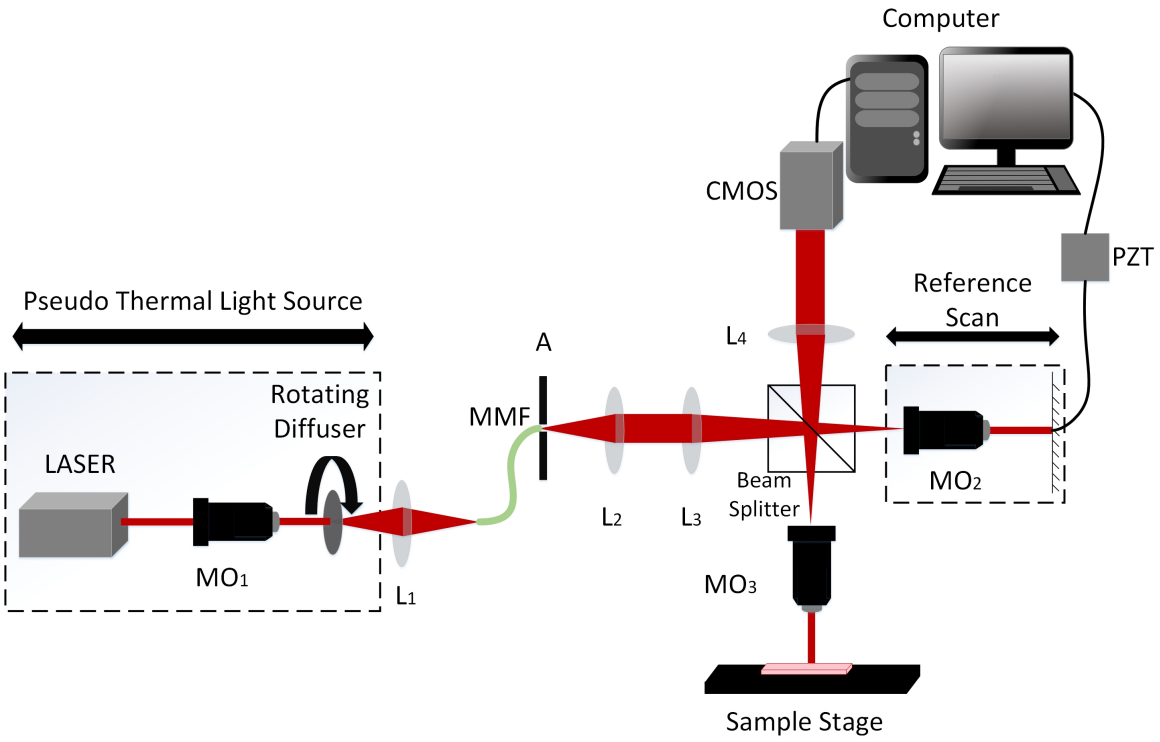

Figure 4.1: Schematic diagram of the Linnik setup with a PTLS to acquire the quantitative phase maps of bacteria cells sample. (*RD*-rotating diffuser, *L*- lens, BS-beam splitter, *MO*-microscope objective, *MMFB*- multiple multimode fiber bundles).

4.5 Processing steps of recorded interferograms

Following processing, steps are adopted for data analysis.

(1)Phase recovery using *MATLAB* and *PCA* [38] algorithm explained in *Section 2.2.2.*

(2) Phase Unwrapping

(3) Higher-order aberration removal

(4) Splitting of entire *FOV* in smaller cells.

(5)Defocus correction using algorithm explained in *Section 2.3* and Image segmentation to achieve a single bacteria cell.

(6) Conversion the phase information of single bacteria into *OPD* information using Eq.1.15.

(7) Measurement of morphological parameters using *OPD* information obtained and formulas discussed in Section 4.7 using *MATLAB*.

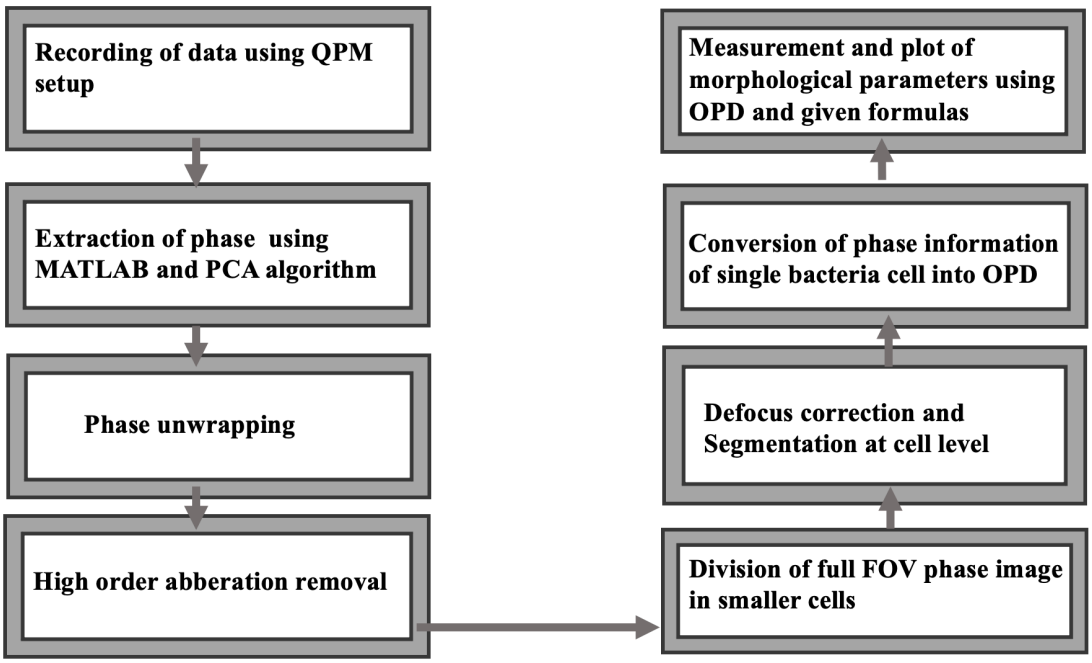

Figure 4.2: Block diagram to show step-by-step processing steps starting from recording the data ending up on measurement of morphological parameters.

4.5.1 Phase recovery and unwrapping

PCA [38] was used to extract the phase information. Figure 4.3b depicts one of the recorded interferograms utilized to extract amplitude and phase information, as illustrated in Fig. 4.3c. Fig.4.3d is the reconstructed wrapped phase map(2304X2304 pixels).

Without processing, the phase measurements cannot differentiate between particular phase values, say ϕ, and a value such as $\phi + 2\pi$ or $\phi + 4\pi$ [8]. So instead, the measurement is stated to produce wrapped phase information. In other words, the phase measurements return values within the $[-\pi, \pi]$ interval [8]. Beyond the $[-\pi, \pi]$, the recorded phase signal can be mathematically corrected to span large intervals. This process is called phase unwrapping [8][45]. In Fig.4.4' dash line' represents the wrapped phase, and the dotted line represents the phase after unwrapping.

Wrapped phase images can be generated by a variety of technologies such as synthetic aperture radar *(SAR)*, magnetic resonance imaging *(MRI)*, and fringe pattern analysis are a few examples [8][45]. Unfortunately, the wrapped phase images generated by these technologies are unreadable unless they are first unwrapped to make a continuous phase map [8][45].

A phase unwrapping algorithm identifies the presence of a phase wrap in an image by computing the difference between two successive samples, and it can perceive noise as a phase wrap. If this difference is more significant than $+\pi$, the phase unwrapping algorithm perceives this region to be wrapped. Due to noise, this might either be an actual phase wrap or a false wrap. While working with phase images, it is crucial to record data carefully and

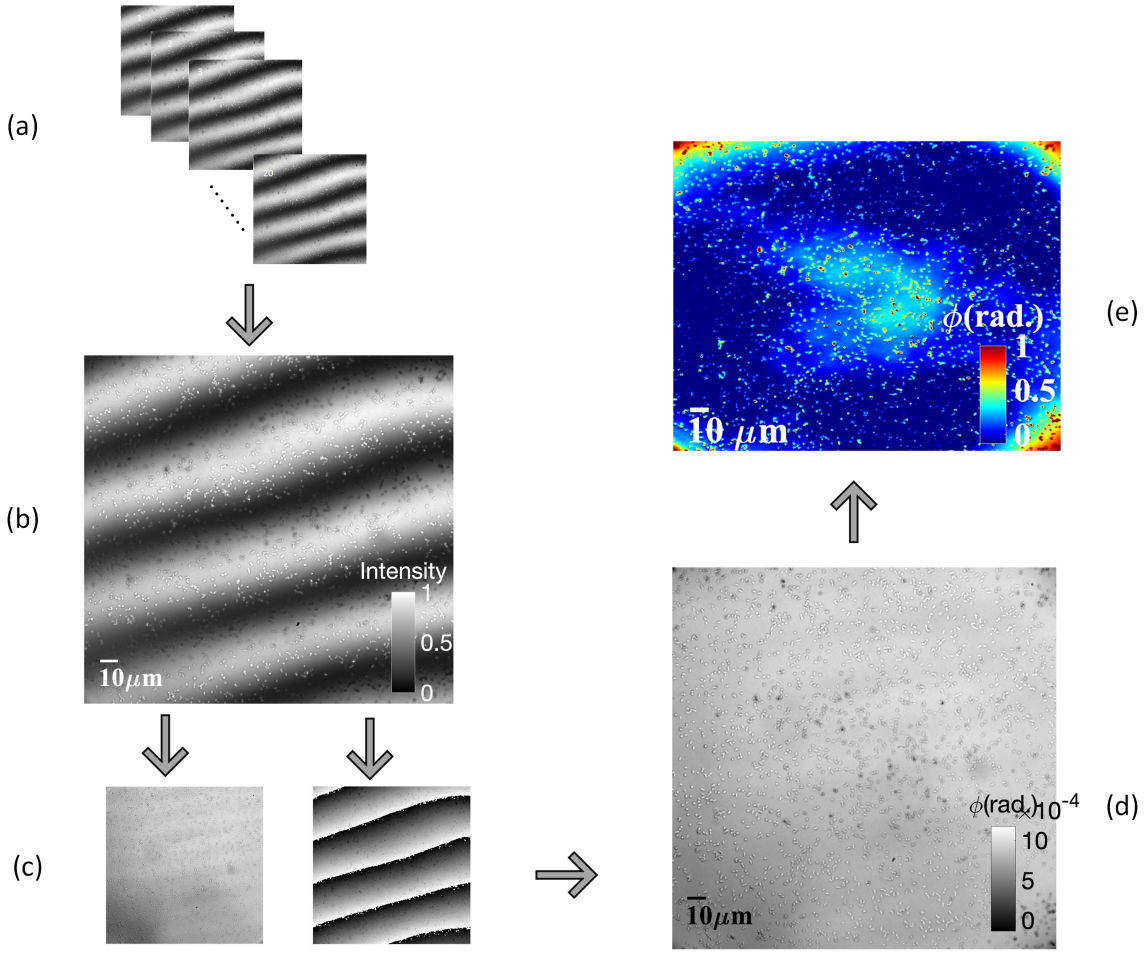

Figure 4.3: Step by step process of phase extraction (a)Schematic illustration of 20 frames of recorded interferogram(b)one of the 20 Interferogram (c) Amplitude and phase information extracted using *PCA* (d) Reconstructed unwrapped phase information (e) Phase image after unwrapping and tilt removal.

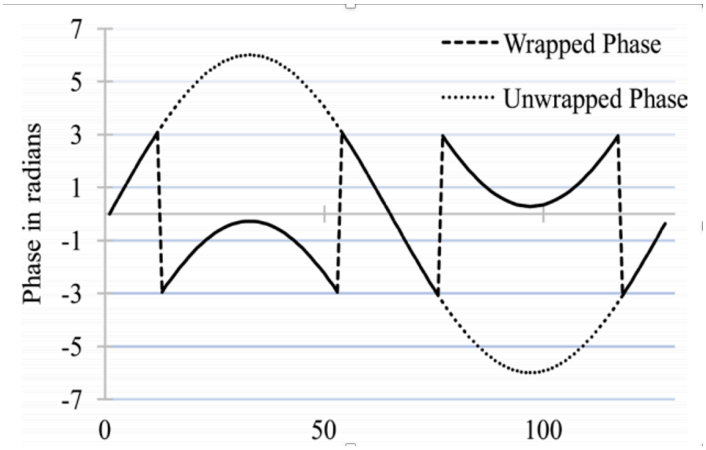

Figure 4.4: Visual comparison of wrapped and unwrapped phases is shown. The 'dash line' represents the wrapped phase, and the dotted line represents the after unwrapping [45].

work in an environment where no movements and vibrations can cause noise in the images. Therefore, it is best to conduct experiments carefully on a vibration isolated optical table.

Unwrapping these phase maps using the minimum L^p-norm 2D phase unwrapping algorithm [53], as shown in Fig.4.3e., and the *MATLAB* code was provided by my supervisor Azeem Ahmed.

4.5.2 Higher-order aberration removal

The defocus corrected unwrapped phase maps obtained in the previous step are corrupted with the higher-order phase aberration. Therefore, removing the aberration effect from the phase images is necessary before quantifying morphological and statistical parameters. The background phase error is not part of the sample phase maps and is due to higher-order phase aberration in any optical system. In reality, all the phase microscopy systems suffer from the aberrations caused by imperfect optics used to develop the system. As high order phase aberrations are not part of the specimen's phase maps, removing such errors for the recovered phase maps with minimal phase errors is mandatory.

The background related to the higher-order aberration is estimated using the inbuilt *MATLAB* function file *'strel*,' which represents a morphological structuring element. The structuring element is considered disk-shaped. The disk radius is considered to be greater than the approximate average size of all the bacteria present in a *FOV*. In our case, the disk radius equal to 30 pixels is optimal for the background detection. The measured background is further subtracted from the bacteria phase map to remove higher-order phase errors. The extracted phase was processed further.4.5a. The unprocessed phase map consists of significant higher-order phase aberration. Therefore, image morphological operations were used to eliminate the higher-order phase aberrations. The results from these two relatively simple operations provided satisfactory results in Fig.4.5b.

(a) (b)

Figure 4.5: Illustration of Higher-order aberration removal through morphological operations (a)Before (b) after.

4.5.3 Segmentation of entire *FOV* and its splitting into smaller cells

We did image segmentation twice. First, it was done over the whole *FOV*. The complete *FOV* phase image was converted into a binary mask eliminating undesirable and bulging bacteria using a threshold. Further, the connected components algorithm was used to determine the location of each object(bacteria) in the binary mask using the *MATLAB* command *'regionprops'* to measure the extrema of each bacteria. These locations were then referenced with the phase image to extract single bacteria and place it in a separate image. However, this technique has its limitations. For instance, we can ensure that each image would have at least one complete bacteria. Still, we might have some partial or even complete unwanted bacteria along with the bacteria we were initially interested in. This happens because *'regionprops'* while measuring the extrema of each connected object returns us the minimum and maximum range of pixels along both the x and y-axis and other bacteria may lie in the same region as well. This problem has been later addressed in *Section 4.5.5*.

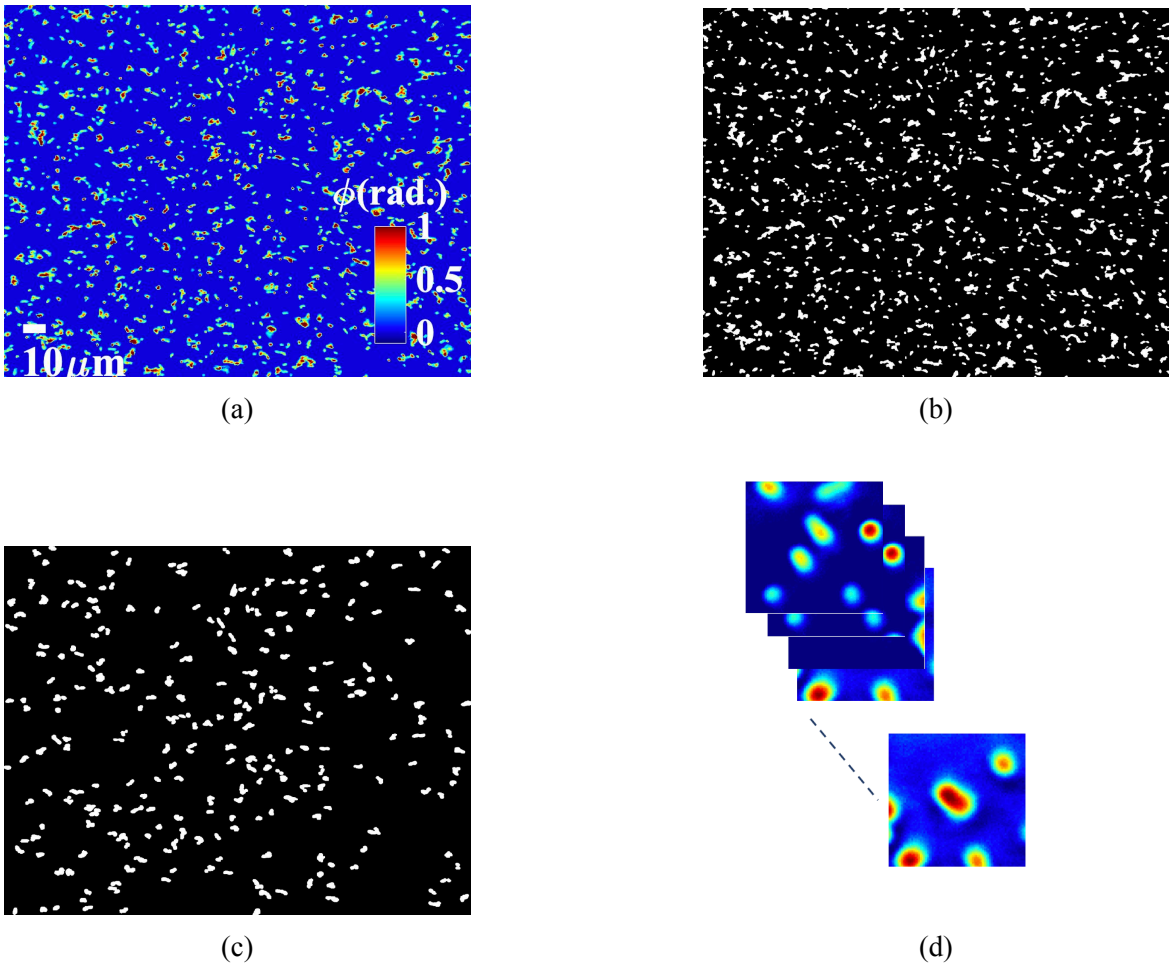

(a) (b)

(c) (d)

Figure 4.6: Splitting the full *FOV* phase image into smaller cells was done by developing a mask using the image itself and removing unwanted and bulge of Bacteria through a threshold. (a)Reconstructed phase image (b) Binary image of reconstructed phase image(c) Binary image after removing unwanted and bulge of Bacteria (d) Schematic representation of smaller cells obtained at this step.

4.5.4 Defocus correction and segmentation at the cell level

The defocus correction at the cell level is crucial, as for each cell, the defocus amount is different and needs to be corrected. One can propagate the field to various planes in a range of -r to+r where r is the expected defocus. The variance of amplitude at these positions vs. position gives a sharpness curve. The sharpness curve is a plot of amplitude variance as a function of propagation distance. The minimum point at the sharpness curve gives the defocus amount in that image. The objective lens's actual focal plane is where amplitude variation gives a minimum. Fig. 4.7a represents the reconstructed phase image. The sharpness curve depicts the change of amplitude variance w.r.t propagation distance 'z.' As shown in Fig. 4.7b, the sharpness curve has the dip at d =-1.3 μm, which indicates the objective lens's actual focal plane. In a nutshell, this value is the quantification of defocus amount [19].

After defocusing correction, we segment our data sets at the cell level. The bacteria cells were made perfectly isolated in an image so that the statistical analysis is reliable.

Our primary expectation from segmentation is the noise-free image and only retains well-shaped and well-imaged bacteria. On top of it, the overlapping bacteria, bacteria clusters should be discarded as they can skew the statistical values for parameters of bacteria. The first step was by creating a mask out of the image itself. Then, the image was thresholded. The thresholding of the phase images is done by measuring the system's peak to valley phase sensitivity. The threshold phase value is considered 1.2-1.4 times the system's peak to valley phase error for the bacteria segmentation. This threshold value is an optimum value for the segmentation as maximum phase values of most bacteria are approximately more significant than 3-4 times of the peak to valley phase error. Next, the segmented areas of an image are further dilated by 4 pixels along all sides to remove any chances of bacteria crop. The generated binary image is then multiplied by the recovered phase image. Therefore, the defocused phase information is corrected by propagating the complex field from the region or plane (reconstructed) to the objective lens's focal plane [19]. Fig. 4.7c is a numerically focused image that is again having artifacts. Moreover, Fig. 4.7c has more than one bacteria, and we are attempting to acquire a single bacteria cell in an image to achieve trustable quantitative analysis. Fig. 4.7d is the binary image of Fig. 4.7c. Fig. 4.7e is the single bacteria binary image obtained through segmentation. From Fig. 4.7f, it is visible that bacteria cells are getting focused. Some of the bacteria cells are removed from the image through segmentation because we wanted to have a single bacteria cell in an image to have accurate quantitative analysis. That is why we only selected images containing single bacteria cells to calculate morphological parameters.

In Fig.4.8 different bacteria cells are shown before and after defocus correction and segmentation. Fig. 4.8a figures represent reconstructed phase images of bacteria cells on the left side. Fig. 4.8b represents the numerically focused phase image. As shown in Fig.4.8b,

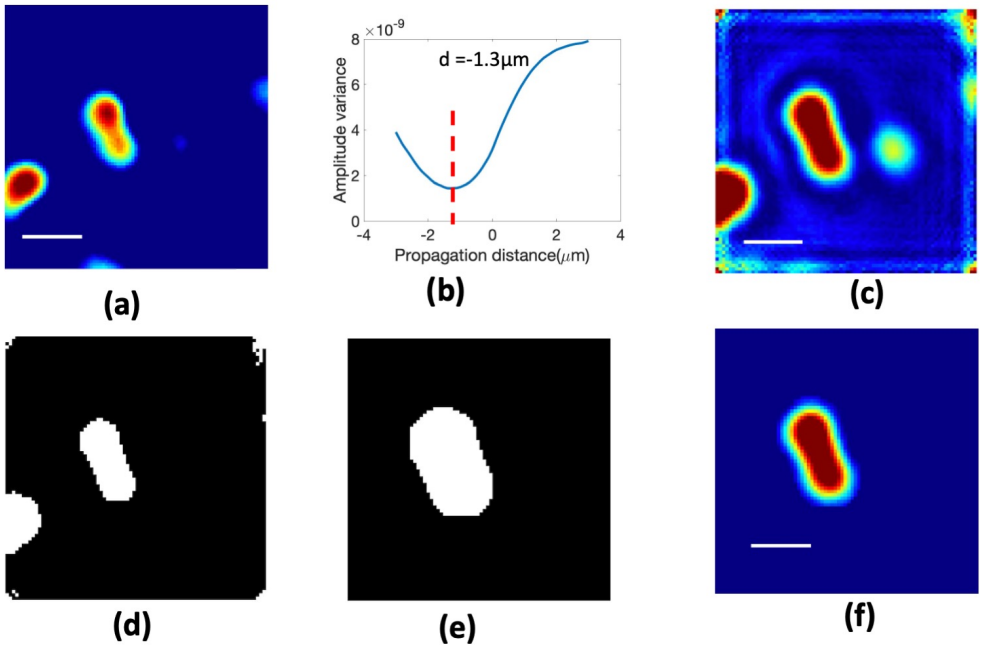

Figure 4.7: Defocus Correction of *E. coli* at single-cell level imaged by 660nm *PTLS* using 60x/1.2 *NA* objective lens(a)Reconstructed phase image before focus correction(b)sharpness curve to estimate the amount of defocus in the idea that is -1.3μm in this image (c) Numerically focused image (d) Binary image of numerically focused image (e) Binary image of single bacteria (f) Segmented and numerically focused image acquired by multiplying image (e) with an image (c).

the defocus correction algorithm produces artifacts around the boundaries of cells that are not part of the image, So it is crucial to remove them using segmentation.

Here in Fig. 4.8c is the binary image of image Fig.4.8b.Fig.4.8d represents the single bacteria binary image obtained by segmenting it. Finally, fig. 4.8e is the product of phase and single bacteria binary image to get a single bacteria per cell.

The bacteria cells that were perfectly isolated were chosen equally for both wavelengths. The single bacteria cell images used for statistical analysis were 1332 for *Ecoli-1*, 1026 for *Ecoli-2*, 1577 for *K. pneumonia*, and 1806 for *K. pneumonia*. We compared the morphological parameters using *PTLS* of wavelength 532nm and 660nm. The number of cells was equal for the two wavelengths.

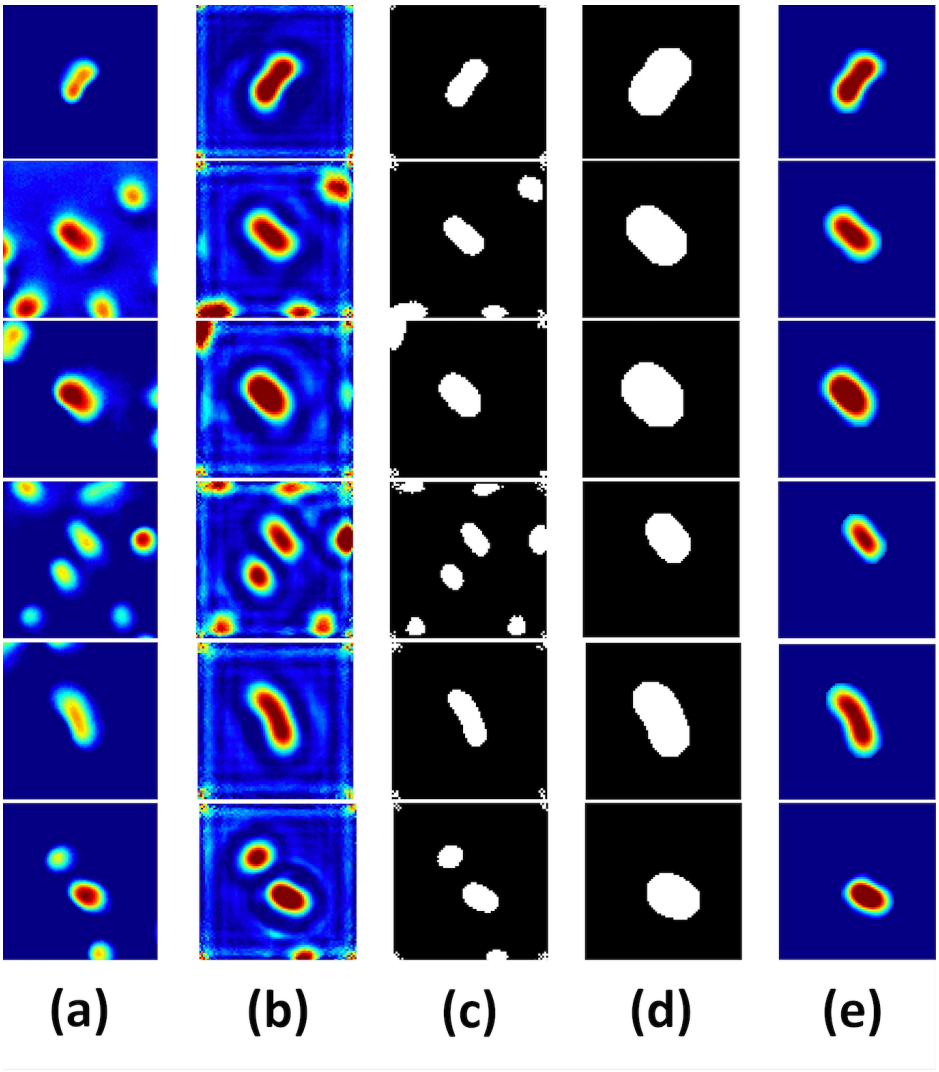

Figure 4.8: Effect of defocus correction algorithm and segmentation on different bacteria cells (a)Reconstructed phase image (b) Numerically focused phase image (c) Binary image of numerically focused image (d) Single bacteria binary image (e) Multiplication of phase and binary image.

4.5.5 Morphological parameters and their formulas

Following parameters were used for quantitative analysis of bacteria cells.

Phase volume

Phase volume is the equivalent of cell volume directly based on phase information and takes refractive index variations within the cell into account [33]. The phase volume is related to the cell's dry mass.

$$V = \int_P OPD \, ds \tag{4.1}$$

Phase surface area

This metric may be computed as the sum of the projected area and the phase profile's top surface area.

$$SA = \int_P dA + P \tag{4.2}$$

$$SA = \int_P \sqrt{(1 + \delta h_x^2 + \delta h_y^2)}\, dxdy + P \tag{4.3}$$

dA =The discrete cell surface area projected over a single camera pixel
δhx and δhy= The gradients along the x and y axes of the cell *OPD* map [46, 47].
dx and dy= Calibrated pixel width along the x and y-axis.

Phase surface area to volume ratio

This quantity reflects phase variations in the cell.

$$SAV = \frac{SA}{V} \tag{4.4}$$

Projected area to volume ratio

This property specifies the cell's flatness [33].

$$PAV = \frac{PA}{V} \tag{4.5}$$

Phase sphericity index

This value expresses the measure of roundness of the cell. An object's sphericity is defined as the ratio of its volume to its surface area. The value of a round shape may indicate cell abnormalities [33, 49–51].

$$\Psi = \pi^{\frac{1}{3}} . \frac{(6 * V)^{\frac{2}{3}}}{SA} = 4.84 * \frac{(V)^{\frac{2}{3}}}{SA} \tag{4.6}$$

It is a dimensionless constant with values ranging from 0 for a flat disk to 1 for a spherical shape [50].

Energy

Energy describes the texture of the cell [33].

$$E = \sum_{i=1}^{n} OPD(i)^2 \tag{4.7}$$

Entropy

The concept of phase entropy is presented as a way to quantify 2-D phase space. The rate of variability and diversity of the phase distribution is depicted by entropy [52].

$$Entropy = -\sum_{i=1}^{n}(p(OPD_i)(log_2 p(OPD_i) \tag{4.8}$$

Phase mean

The mean is the average of the phase values of a group of cells [33].

$$\mu = \frac{\sum_{i=1}^{n} OPD(i)}{n} \tag{4.9}$$

Phase variance

This metric quantifies the dispersion of a collection of phase values of the cell [33].

$$\sigma^2 = \frac{\sum_{i=1}^{n}(OPD(i) - \mu_{OPD})^2}{n} \tag{4.10}$$

Phase kurtosis

Phase kurtosis determines whether the phase distribution of the cell is flat or peaked [33].

$$Kurtosis = \frac{\sum_{i=1}^{n}(OPD(i) - \mu_{OPD})^4}{\sigma^4} \tag{4.11}$$

Phase skewness

Phase skewness is a metric that measures how a cell's *(OPD)* values differ from the average value [33].

$$Skewness = \frac{\sum_{i=1}^{n} OPD(i) - \mu_{OPD})^3}{\sigma^3} \tag{4.12}$$

4.5.6 Statistical analysis

We obtained 11332, 1026, 1577, and 1806 *OPD* maps for bacterium cells for *Ecoli-1*, *Ecoli-2*, *K. pneumonia*, and *K. pneumonia*, respectively. We utilized the two-sample t-test for the *p-values* of the data to analyze statistical differences across the cells, for derived parameter each bacteria cell line at the two wavelengths (532 nm and 660 nm).

Table 4.2: Morphological parameters and their formulas

Parameter	Definition
H(OPD)	$h(x,y)\Delta n = \frac{\lambda}{4\pi} * \phi(x,y)$
Surface Area(µm^2)	$SA = \int_P dA + P$
Volume	$V = \int_P OPD\, ds$
Mean	$\mu = \frac{\sum_{i=1}^{n} OPD(i)}{n}$
Variance	$\sigma^2 = \frac{\sum_{i=1}^{n} OPD(i) - \mu)^2}{n}$
Entropy	$Entropy = -\sum_{i=1}^{n}(p(OPD_i)(log_2 p(OPD_i)$
Kurtosis	$Kurtosis = \frac{\sum_{i=1}^{n}(OPD(i) - \mu_{OPD})^4}{\sigma^4}$
Skewness	$Skewness = \frac{\sum_{i=1}^{n}(OPD(i) - \mu_{OPD})^3}{\sigma^3}$
PAV	$PAV = \frac{PA}{V}$
SAV	$SAV = \frac{SA}{V}$
Sphericity	$\Psi = \pi^{\frac{1}{3}} . \frac{(6*V)^{\frac{2}{3}}}{SA} = 4.84 * \frac{(V)^{\frac{2}{3}}}{SA}$

4.6 System Characterization

In any *QPM* setup, higher temporal and spatial phase sensitivity is mandatory for the accurate quantification of phase maps. In addition, the temporal phase sensitivity gives interferometer stability, contributing to biological cell membrane fluctuation measurements. Moreover, this can be achieved using a high temporal coherent laser. However, the high coherent light source can reduce the spatial phase sensitivity. In addition, interference with multiple reflections from optical surfaces and light scatter due to dust particles degrades image quality and ultimately appears in-phase images. So, the spatial phase sensitivity of *QPM* systems restricts their phase measurement precision.

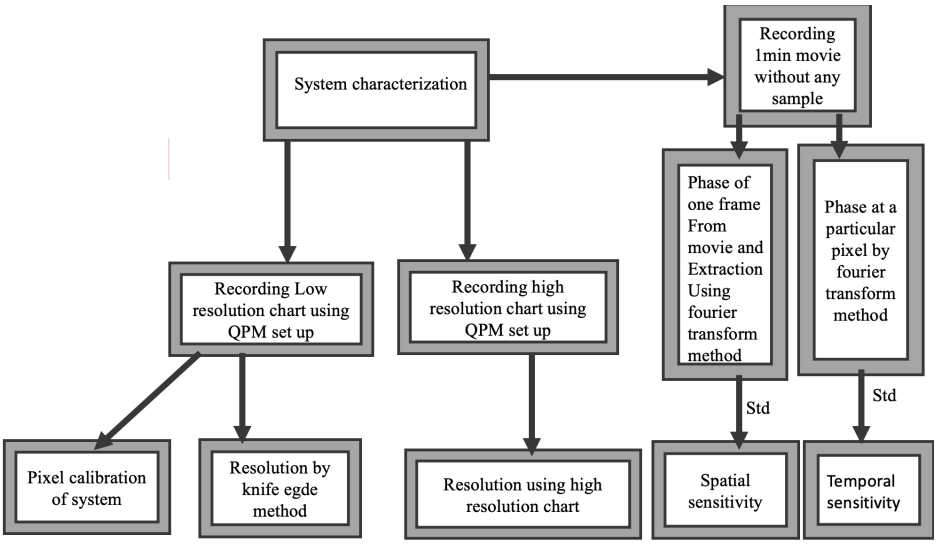

Figure 4.9: Block diagram of all steps done for characterization of the system.

4.6.1 Pixel calibration of the system

The acquired results of images are usually in pixels. We can convert them into length units by using a calibration factor. We can calibrate the system using a low-resolution chart, as shown in Fig.4.10a First, we captured an image of a *standard USAF chart* using an objective lens of 1.2 NA water immersion (60×) and wavelength 638 nm. Then the line profile of the *USAF chart* on a specific region shown by the yellow line is plotted and shown in Fig.4.10b.

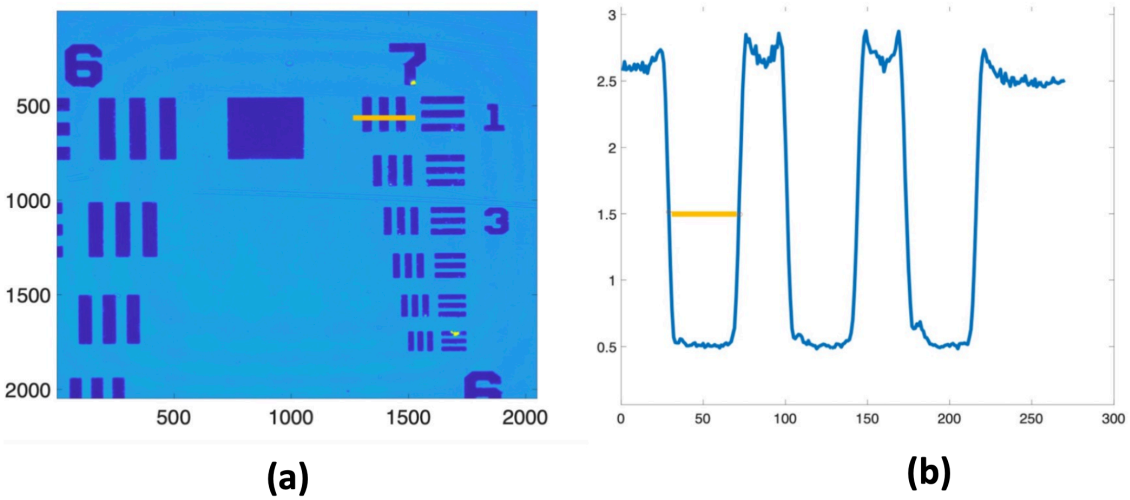

Figure 4.10: Pixel calibration of the Linnik interferometer-based *QPM* system(a) *USAF* low-resolution chart with a yellow line showing one of the regions selected and (b) its line profile. The width of a yellow line on line profile will give results in pixels, and for comparison, the width of the same line in micrometers can be obtained *USAF Resolving Power Test Target 1951*[48]. On comparing these two results calibration factor was estimated as 89nm.

The width of the line in Fig.4.10b is found to be 44pixels. The width of the same line in micrometer using *USAF resolving power test target 1951*[48] with group number 7 and element number 1 is found as 3.91 micrometers.

$$3.91\mu m = 44pixels \tag{4.13}$$

$$1pixel = 0.0888\mu m = 88.8nm \tag{4.14}$$

This process was repeated several times at different positions, and the average result for the calibration factor was found as

$$1pixel = 0.091\mu m = 91nm \tag{4.15}$$

4.6.2 Measurement of temporal phase sensitivity

The temporal sensitivity specifies the minimum detectable phase value as a function of time as discussed in *Section 1.6.1*. The interferometer type determines the temporal phase stability,i.e., whether it is a common or non-common path interferometer [8]. We imaged a silicon wafer without any sample and recorded a 1-minute time-lapse interferometric video in a stable environment to assess the current *QPM's* spatial and temporal phase sensitivity. As explained in *chapter 2*, the *Fourier transform approach* is then used to extract phase maps for the whole interferometric video. The change in phase value of a particular pixel as a function of time measures the system's temporal phase sensitivity. The setup's temporal phase noise is independent of the light source's coherence length. Therefore, it is solely dependent on the interferometer's stability. Fig.4.12 (a) depicts the setup's temporal noise as a function of time. Fig. 4.12 (b) illustrates the setup's temporal noise as a function of time.

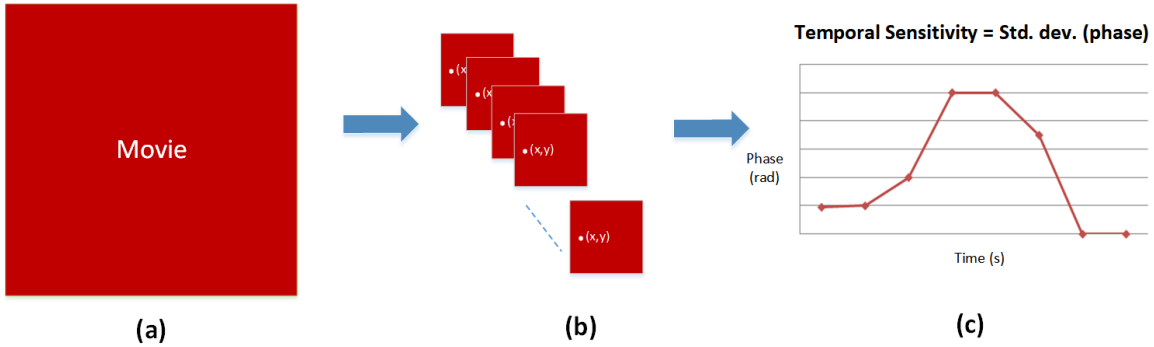

Figure 4.11: Schematic representation of the process to find temporal sensitivity (a) A 1-minute movie is recorded using the *QPM* setup. (b) A pixel is selected on all of its frames (c). The phase values of selected pixels are found and plotted as a function of time; it represents phase noise. The standard deviation of phase represents temporal sensitivity.

Fig. 4.12 (b) shows phase variation with time. It contains 800-time points with a temporal step size of 12 fps ($\approx 80ms$) at the center of the interferogram (256,256). As a result, the temporal phase stability is about 38 mrad, equating to a 1.9nm sensitivity in temporal height measurement.

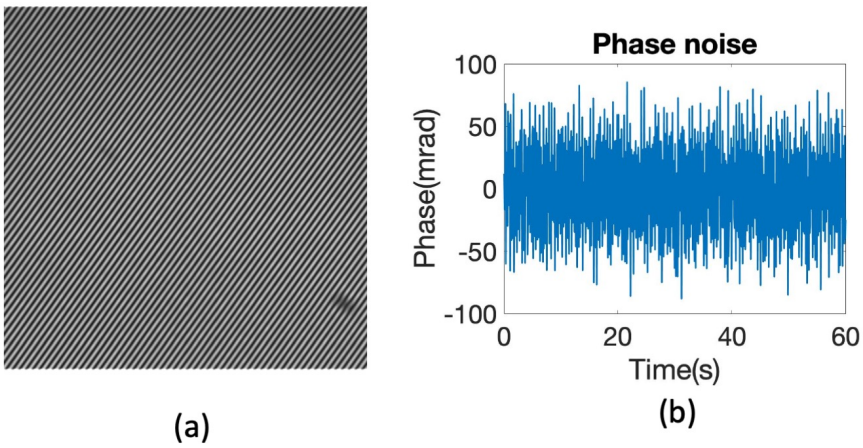

Figure 4.12: Determination of *QPM's* temporal phase sensitivity(a) interferogram produced while using a Si substrate as a test specimen (b) temporal phase noise or phase variation with time.

4.6.3 Measurement of spatial phase sensitivity

The spatial phase sensitivity of the system defines the minimum spatial phase variations due to either refractive index or height that the system can detect as discussed already in *Section 1.6.2* [8]. One of the interferograms from the recorded movie used to determine Temporal phase sensitivity can measure the system's spatial phase noise. Fig.4.13a and 4.13b shows the interferogram and the recovered phase map, and Fig. 4.13c shows the corresponding histogram, respectively. The system's spatial phase noise was measured by measuring the standard deviation of the reconstructed phase values and is 5.6 mrad.

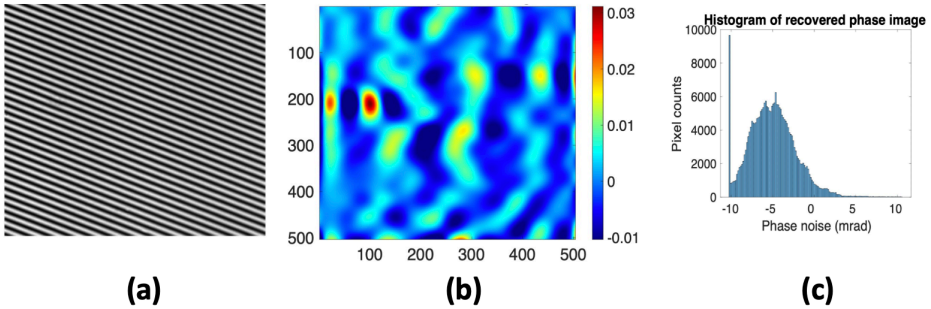

Figure 4.13: The process to find the spatial sensitivity of the Linnik based *QPM* system. (a)Recorded interferogram and (b)its respective reconstructed phase image. (c)Histogram of recovered phase image. The system's spatial phase noise was measured by measuring the standard deviation of the reconstructed phase values and is 5.6 mrad.

4.6.4 Resolution measurement of the system by the knife-edge method

The slanted knife-edge approach can estimate the resolution of the setup [44]. It was calculated by choosing any line on the *USAF chart* and plotting a line profile from the center of the dark line to the center of the adjacent line, as shown in Fig. 4.14a by yellow region on the *USAF chart*. Fig. 4.14b shows the line profile of the yellow region. Fig. 4.14c represents the plot of differential of line profile respectively whose full-width half maximum *(FWHM)* is 6 pixels. It is $0.5387\mu m = 538.7nm$ in length dimensions. Therefore, using the formula, the theoretical resolution (calculated value of lateral resolution) is 275nm.

$$d = \frac{\lambda}{2NA} = \frac{660}{2X2.4} = 275nm \tag{4.16}$$

where λ= $660nm$ and $NA = 1.2$

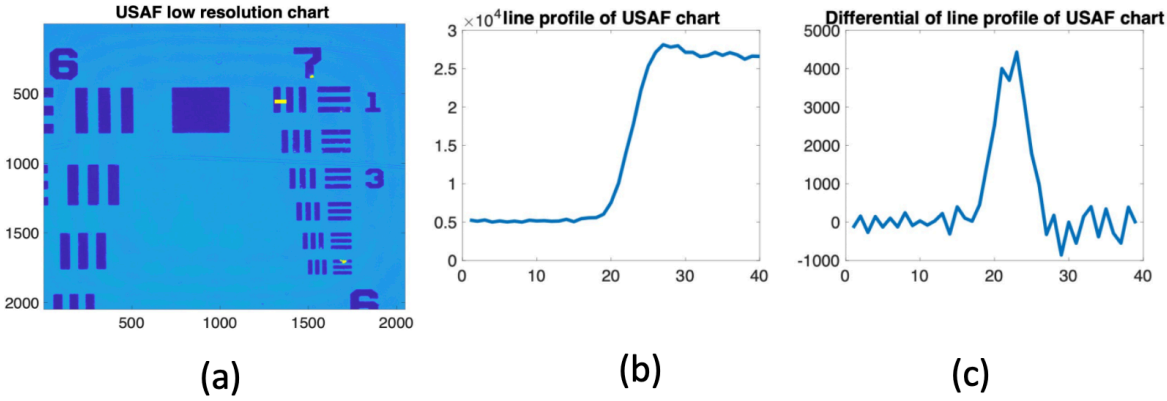

Figure 4.14: Step by step process for resolution measurements using Knife-edge method. (a)USAF low-resolution chart with a highlighted yellow region. (b)The line profile of the highlighted region is shown in(a) and the differential of the line profile. *FWHM* of the differential profile was found as 6 $pixels$, and in microns, it is seen as $0.546\mu m = 546nm$. This process was repeated at several points, and average*FWHM* was found to be 5.6 $pixels$ and $509.6nm$ in length dimensions that gives an estimated resolution.

4.6.5 Image of a high-resolution chart recorded by an objective lens with a magnification of 60X and a *NA* of 1.2.

A high-resolution chart can also determine the resolution of a setup. For example, the image in Fig.4.15 is a high-resolution chart recorded by an objective lens with a magnification of 60X and a *NA* of 1.2. The resolved bar number on the high-resolution chart is 1400

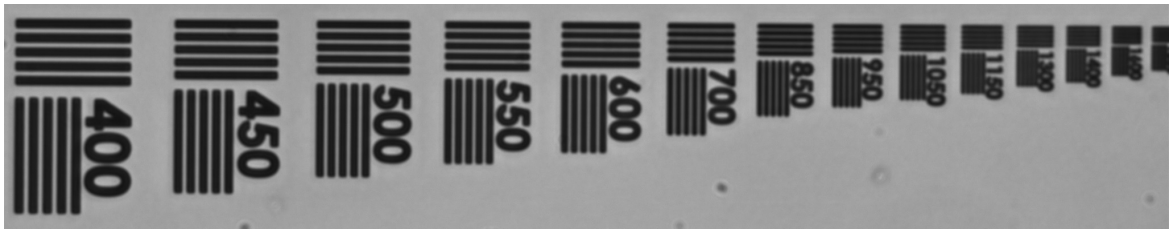

Figure 4.15: Resolution using the high-resolution chart.

$$Barnumber = 1400 linepair/mm \tag{4.17}$$

$$Barwidth = \frac{1}{1400}.mm/linepair \tag{4.18}$$

$$Barwidth = \frac{1000}{1400}\mu m/linepair = 0.714\mu m/linepair \tag{4.19}$$

$$= \frac{0.714}{2}\mu m/line = 0.357\mu m/line = 357nm/line \tag{4.20}$$

The measured lateral resolution was obtained to be 357 nm.

Chapter 5

Results and Discussion

5.1 Comparison between Laser and pseudo thermal light source

Laser has high temporally and spatially coherent properties. Coherent noise and parasitic fringe production caused by several reflections from various regions of the optical components significantly degrade image quality. As an outcome, the system's spatial phase sensitivity is reduced [4][9]. However, as the coherence length of the *Laser* is large (e.g., 20-100 cm), it is experimentally easy to obtain the interference fringes. On the contrary, broadband light sources such as white light and $LEDs$ are utilized to improve the phase sensitivity and measurement accuracy of *QPM*. Due to their lower temporal coherence length, such light sources allow high spatial phase sensitivity compared to *Laser*. However, it is well known that the interference occurs whenever the *OPD* between the specimen and the reference beam is within the temporal coherence length of the light source [4]. As a result, generating an interference pattern using such low coherent light sources (coherence length 2-6 μm) is challenging.

Thus, a temporally high coherent and spatially low coherent *PTLS* offers many benefits over conventional light sources. Such sources have been synthesized by sending *Laser* light through a rotating or stationary diffuser and a vibrating multimode fiber bundle $(MMFB)$ [4]. For the spatial phase sensitivity comparison, we recorded interferograms of the bacteria sample using a *Laser* and *PTLS* as shown in Fig.5.1a and Fig.5.1b respectively. The phase map reconstructed using the interferogram recorded by *Laser* is noisy due to coherent noise and speckle noise, as seen clearly from Fig.5.1c. Thus the sample information of the thin specimens like bacteria is embedded in noise and difficult to be recovered. On the contrary, with *PTLS*, one can recover a noise-free phase map.

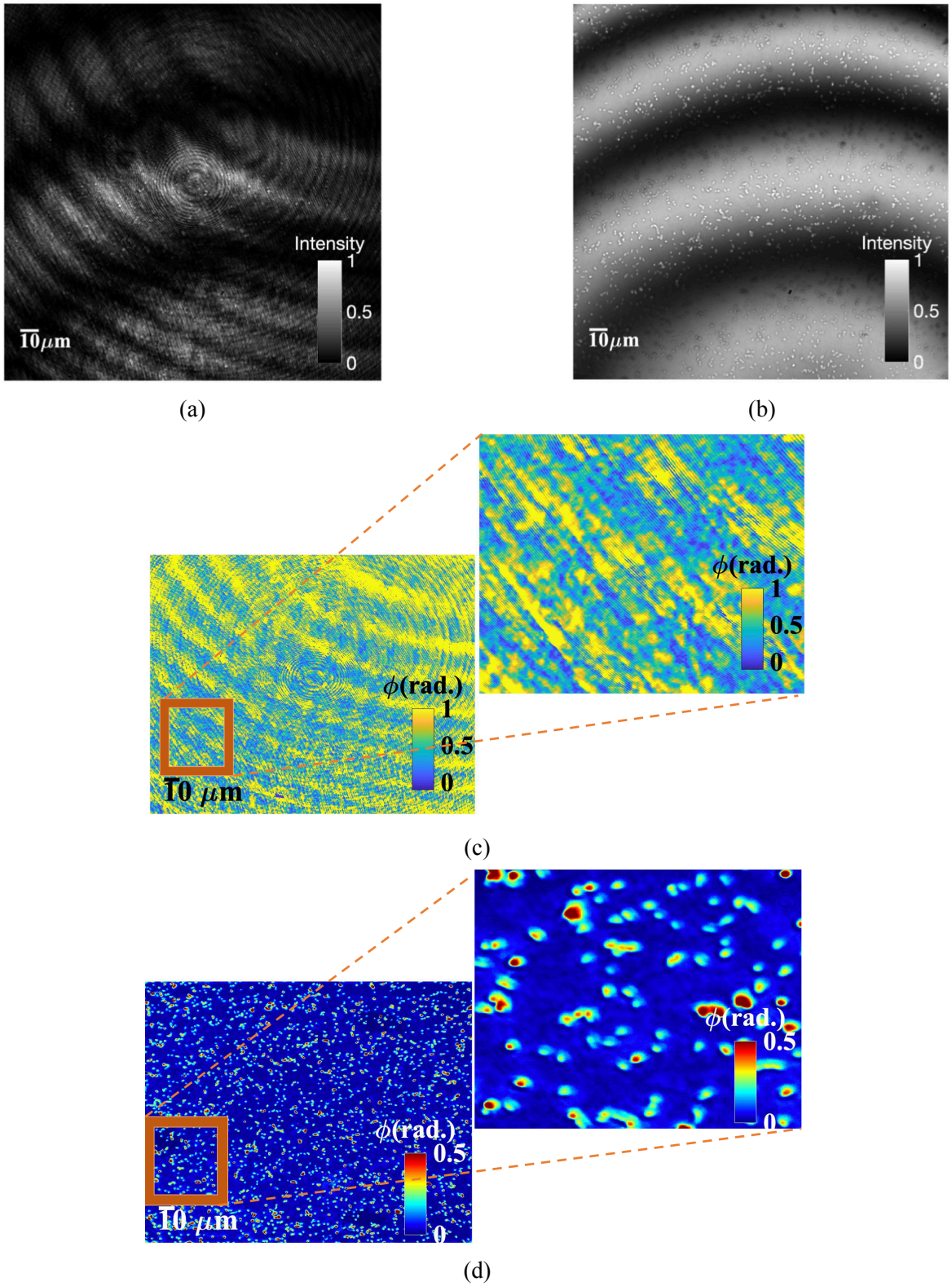

Figure 5.1: Comparison between *Laser* and *PTLS* for imaging in Linnik based *QPM*. Interferogram images of *E. coli* were reproduced using (a) *Laser* and (b) *PTLS*. Reconstructed phase images of *E. coli* were imaged using (c) *Laser* and (d)*PTLS*. The *PTLS* reduces the coherent noise and thus provides high spatial sensitivity.

5.2 Characterization of the morphological parameters of bacteria using a single and the dual-wavelength light source

For the quantitative analysis of the morphological changes happening in the cell, phase maps are usually transformed into *OPD* using Eq.1.13. All the parameters were computed from the *OPD* information. The parameters extracted include surface area (*SA*), volume (V), surface area to volume ratio (*SA/V*), and sphericity *(ψ),* projected area(*PA*), projected area to volume ratio (*PA/V*), energy, entropy, mean, variance, kurtosis, and skewness. These parameters were calculated using the formulas mentioned in the previous chapter.

Whisker box plots were plotted of all the measured values of morphological parameters of each bacteria sample cell. The center lines on the box plot indicate the median, while the 25th and 75th percentiles, or first and third quartiles, are indicated by the bottom and top sides of the box, respectively. The quartiles are the data points that divide the arranged data(ascending or descending order) into four parts. 1st quartile is also called the 25th percentile, and it is a data point that contains 1/4th or 25% data below it. The 3rd quartile is also called the 75th percentile, and it is a data point that includes 3/4th or 75% data below it. Similarly, the central line on the whisker plot represents the median that gives the central value of arranged data. The end of the upper and lower whisker represents the maximum and minimum of the data set, respectively.

The first work of the thesis was to image four bacteria classes using *QPM* at 532 nm and investigate their morphological parameters. To extend this work further, I used another wavelength, i.e., 660 nm, to determine if the bacteria have any spectral signature in the phase map. For such studies, one should have a tunable broadband *Laser* source. However, due to the availability of limited *Laser* sources during my master project, I opted for two different *Laser* sources, i.e., 532 nm and 660 nm. As the refractive index is a function of wavelength, which has both real and imaginary numbers. We hypothesized that some bacteria might have a different response to a change of wavelength, which can be used to pick up a signature. Furthermore, this could change the phase map of the bacteria differently for different bacteria. We tested the hypothesis by experimenting, and our observation is that with the change of wavelength refractive index has changed. So, we can probe the properties which are wavelength dependent. All-optical path length changes by changing the refractive index, and these changes are not linear for all the bacteria.

5.2.1 Phase surface area

The average surface area decreased by 3.7 % for *E. coli-1*. Nevertheless, the mean surface area increased by 3.4%, 0.65 %, and 0.7% for *E. coli-2*, *K. pneumonia*, and *S.aureus*, respectively, on increasing wavelength from 532 nm to 660 nm. The variation in the median of the surface area was also different for each sample. For *E. coli-1*, median surface area decreased, but it increased on switching the wavelength from 532 nm to 660 nm for all other bacteria cells.

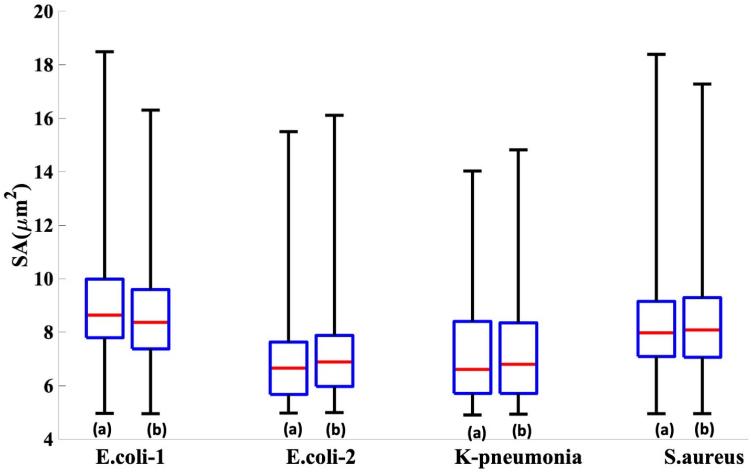

Figure 5.2: Whisker box plot of the surface area of *E. coli-1*, *E. coli-2*, *K. pneumonia* and *S.aureus* (a) at 532 nm (b) at 660 nm. In this plot, it is visible that median was decreased for *E. coli-1* while increased for all other bacteria cells on switching to 660 nm from 532 nm.

5.2.2 Projected area

The average projected area was 0.82 μm^2 for *E. coli-1*, 0.83 μm^2 for *E. coli-2*, 0.81 μm^2 for *k.pneumonia* and 0.77 μm^2 for *S.aureus* at 532 nm. However, the projected area is not changing much on changing the wavelength. All the average values and the standard deviation values of all the parameters are mentioned in *Table 5.1*. The projected area decreased by 1.2% for *E. coli-2* and *K. pneumonia* on increasing the wavelength from 532 nm to 660 nm. On both wavelengths, the median of predicted area values remained constant. However, the distribution of values appeared to be symmetrical for E. coli-1 and asymmetrical for the other bacteria cells.

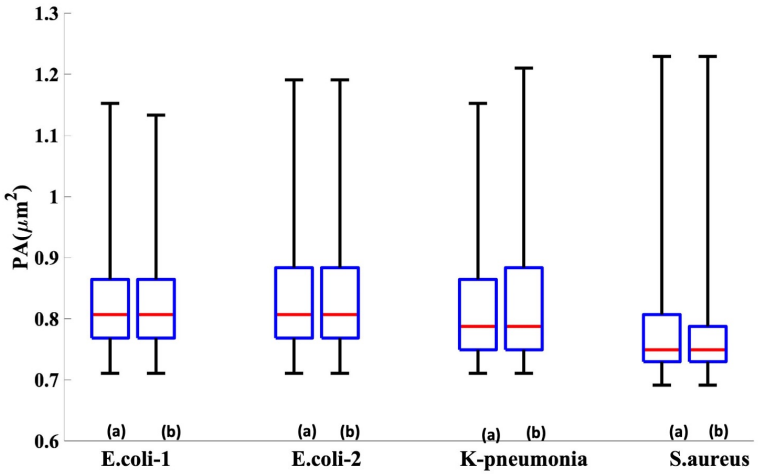

Figure 5.3: Whisker box plot of the projected area of *E. coli-1*, *E. coli-2*, *K. pneumonia*and *S.aureus* (a) at 532 nm (b) at 660 nm. The median of projected area values remained the same on both wavelengths. However, the distribution of values seemed to be symmetrical for *E. coli-1*(median line exactly in the middle) while asymmetrical for all other bacteria cells.

5.2.3 Volume

In Table 5.1 it was shown that for all samples except *S. aureus* average volume is the same 0.1 μm^3. However, median, quartiles, and range increased with an increase of wavelength. For S.aureus, the phase volume is 0.2 μm^3 at both wavelengths.

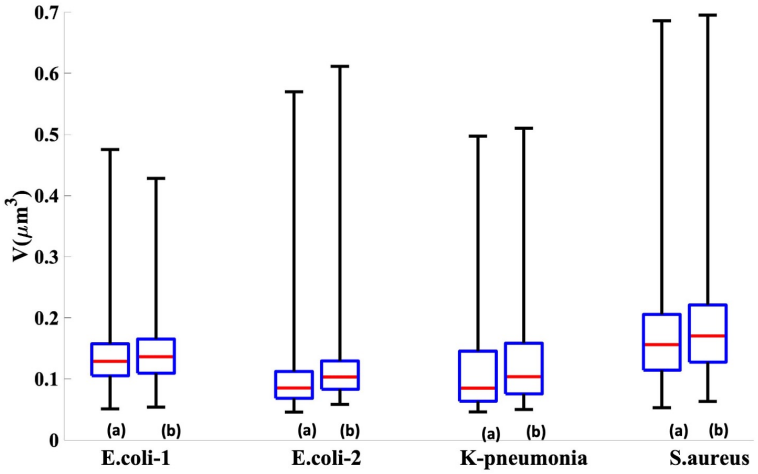

Figure 5.4: Whisker box plot of phase volume of *E. coli-1*, *E. coli-2*, *K. pneumonia*and *S.aureus* (a) at 532 nm (b) at 660 nm. The median and quartiles of phase volume were increased by increasing the wavelength. It reveals that wavelength does affect the phase volume.

5.2.4 Surface area to volume ratio

The surface area to volume ratio decreased with an increase in wavelength. On average *SA/V* ratio was 69 and 63 μm^{-1} for *E. coli-1* in the case of 532 nm and 660 nm, respectively. For *E. coli-2*, the average surface area to volume ratio was 76 μm^{-1} and 66 μm^{-1} in the case of 532 nm and 660 nm, respectively. For *K. pneumonia*, the results indicate that surface area to volume ratio average values were 74 μm^{-1} and 64 μm^{-1} for 532 nm and 660 nm, respectively. In the case of *S.aureus*, the mean surface area to volume ratio at 532 nm and 660 nm were found as 54 μm^{-1} and 49 μm^{-1}. All these results indicated that *SA/V* decreased with the increase of wavelength.

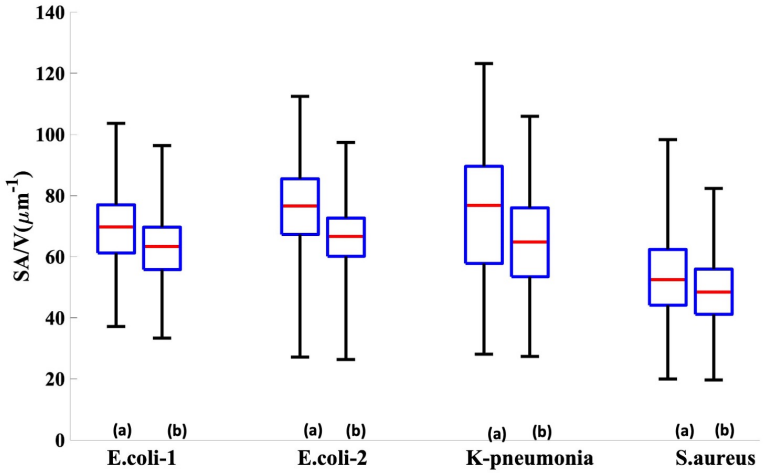

Figure 5.5: Whisker box plot of surface area to volume ratio for *E. coli-1*, *E. coli-2*, *K. pneumonia*and *S.aureus* (a) at 532 nm (b) at 660 nm. The median and quartiles were decreased by increasing the wavelength for all bacteria cells.

5.2.5 Projected area to volume ratio

The projected area to volume ratio results indicated that it was decreased with an increase in wavelength. *PA/V* decreased 6% for *E. coli-1*, 17% for *E. coli-2*, 13.3% for *K. pneumonia* and 10.7% for *S.aureus* . The average *PA/V* was 6.8 μm^{-1} at 532 nm and 6.3 μm^{-1} at 660 nm. For *E. coli-2*, the average *PA/V* values were 9.9 μm^{-1} and 8.2 μm^{-1} at 532 nm and 660 nm, respectively. In the case of *K. pneumonia*, the arithmetic mean of *PA/V* values were 9.3 μm^{-1} and 8.1 μm^{-1} at 532 nm and 660 nm, respectively. Moreover, at 532 nm and 660 nm, the *S.aureus* had an average *PA/V* of 5.5 μm^{-1} and 4.9 μm^{-1} respectively.

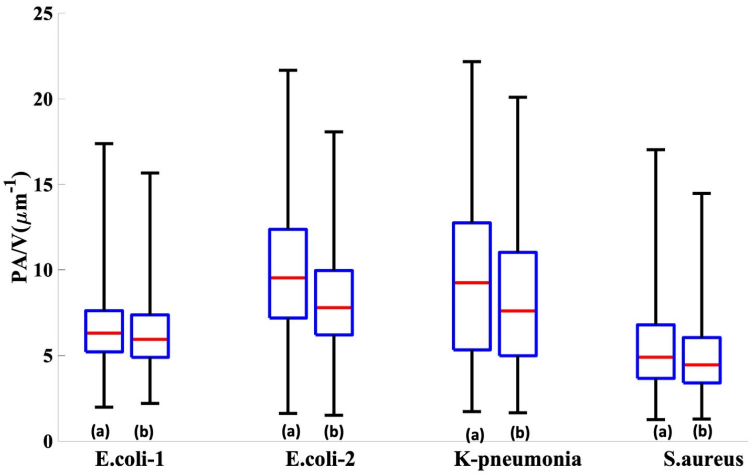

Figure 5.6: Whisker box plot of the projected area to volume ratio for *E. coli-1*, *E. coli-2*, *K. pneumonia* and *S.aureus* (a) at 532 nm (b) at 660 nm. The median and quartiles of *PA/V* decreased with the increase of wavelength from 532 nm to 660 nm.

5.2.6 Sphericity index

The results of sphericity indicated that the mean sphericity increased with an increase in wavelength. It rose 7.59 % for *E. coli-1*, 8% for *E. coli-2*, 8.49 % for *K. pneumonia*, and 5.7 % for *S.aureus* with the increase in wavelength.

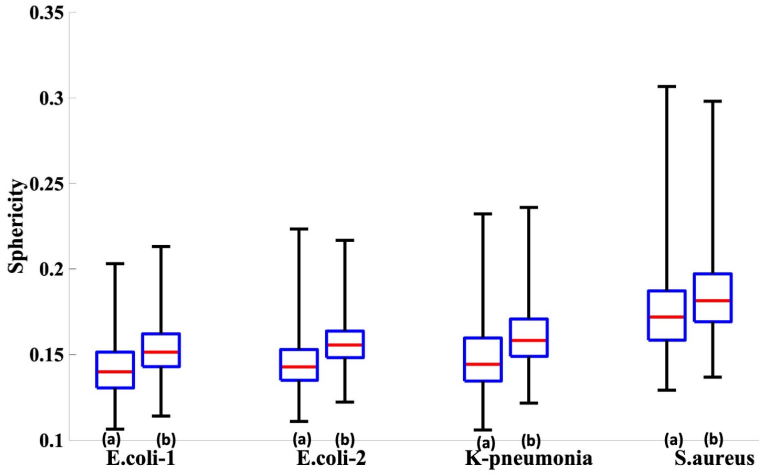

Figure 5.7: Whisker box plot of sphericity for *E. coli-1*, *E. coli-2*, *K. pneumonia*and *S.aureus* (a) at 532 nm (b) at 660 nm. sphericity seemed to be highest for *S. aureus*. Moreover, on switching the wavelength to 660 nm, the sphericity rose. The median and quartiles of sphericity increased by rising the wavelength.

5.2.7 Energy

The average energy increased with wavelength. The mean energy increased 7.5% for *E. coli-1*, 20.5 % for *E. coli-2*, 12.29% for *K. pneumonia*, and 7.97 % for *S.aureus* on changing the wavelength from 532 nm to 660 nm. Moreover, the energy seemed to cover a large range of values compared to all other bacteria cells.

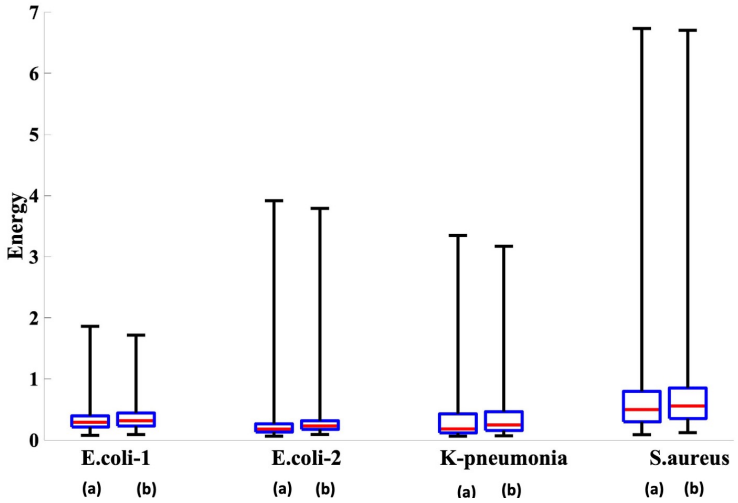

Figure 5.8: Whisker box plot of energy for *E. coli-1*, *E. coli-2*, *K. pneumonia* and *S.aureus* (a) at 532 nm (b) at 660 nm. The median and quartiles of energy remained the same at both wavelengths.

5.2.8 Entropy

The entropy results indicated that average values decreased on increasing wavelength from 532 nm to 660 nm for *E. coli-1*, *E. coli-2*, and *S.aureus* by 2.25%, 1.36%, and 1.34%, respectively. The average entropy seemed to be increasing by 0.6% for *K. pneumonia* on increasing wavelength from 532nm to 660nm. Also, the median of entropy increased for *K. pneumonia* and decreased for the other three cells with increasing wavelength. The arithmetic mean and standard deviation results are shown in *Table 5.1*.

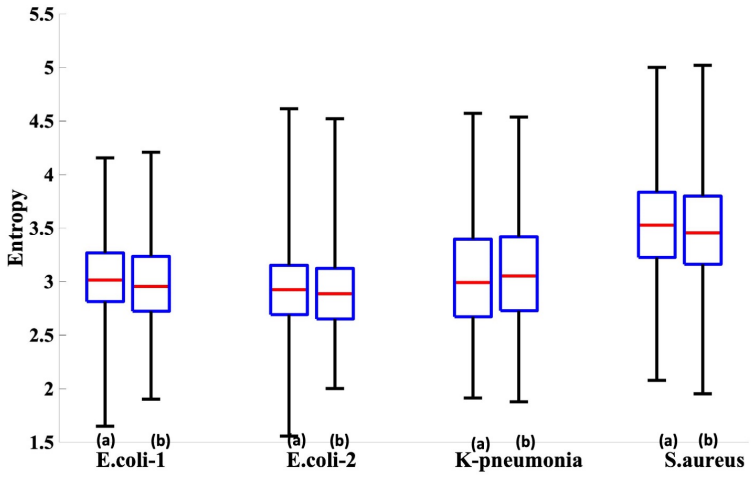

Figure 5.9: Whisker box plot of entropy for *E. coli-1*, *E. coli-2*, *K. pneumonia* and *S.aureus* (a) at 532nm (b) at 660nm. The median of entropy increased for *k. pneumonia* and increased for the other three bacteria cells with the increase of wavelength.

5.2.9 Mean

The mean *OPD* values increased on increasing wavelength as shown in Fig.5.10. The mean increased 9.49% for *E. coli-1*, 13.09% for *E. coli-2*, 12.92% for *K. pneumonia*, and 8.89 % for *S.aureus* on average.

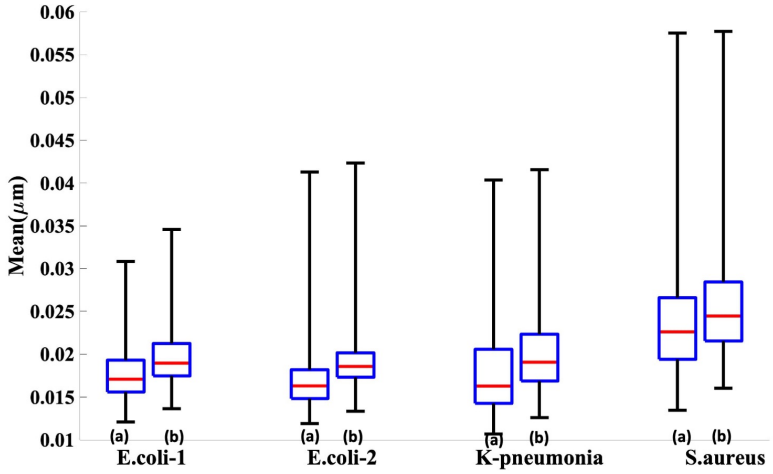

Figure 5.10: Whisker box plot of *OPD* mean for *E. coli-1*, *E. coli-2*, *K. pneumonia*and *S.aureus* (a) at 532 nm (b) at 660 nm. The quartiles and medians of mean *OPD* for all bacteria increased with wavelength shift to a higher value.

The results in Fig.5.11 also indicated that the mean phase decreased with increasing wavelength. In the case of *E. coli-1* phase, on average decreased by 11.4%, for *E. coli-2*, it was reduced by 8.8%, for *K. pneumonia* 9.1% and 12.3% for *S.aureus*. From Fig.5.10 and 5.11, one can observe that the OPD values were increasing with the xtitOPDincrease

in wavelength, but phase values were decreasing. In equation 1.13, it was clear that phase and *OPD* were directly related at a constant wavelength. In our case, the wavelength was not constant; it was varying. Now it depends on the dominant variable and changing the most (wavelength and phase) to decide if *OPD* increased on increasing the wavelength or decreased. Since it was clear from Fig. 5.10 that *OPD* increased the wavelength, it followed the wavelength trend rather than phase. So we can say phase values were changing negligibly compared to wavelength change.

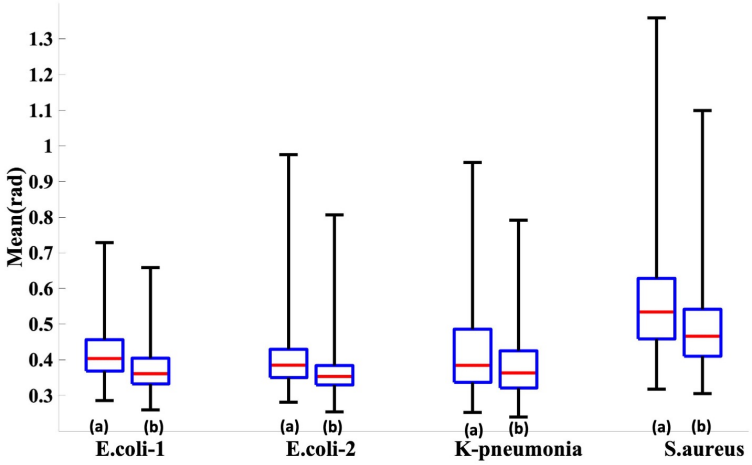

Figure 5.11: Whisker box plot of phase mean for *E. coli-1*, *E. coli-2*, *K. pneumonia* and *S.aureus* (a) at 532nm (b) at 660nm. The mean phase seemed to be decreasing with the increase of wavelength.

5.2.10 Variance

The results of variance indicated minute variation in *OPD* values on average. The average variance for *E. coli-1* was 9.5×10^{-5} and 8.1×10^{-5}, for *E. coli-2* 8.1×10^{-5} and 7.1×10^{-5}, for *K. pneumonia* 12×10^{-5} and 11×10^{-5} and for *S.aureus* 26×10^{-5} and 22×10^{-5}at 532 nm and 660 nm respectively. The average variance seems to be increasing by 15 % for*E. coli-1*, 12.42% for *E. coli-2*, 8.12 % for *K. pneumonia* and 11.68 % for *S.aureus* on increasing wavelength from 532 nm to 660 nm.

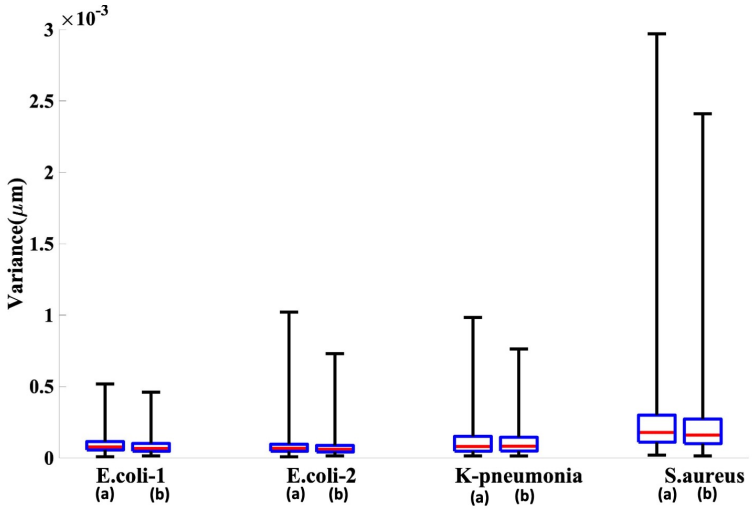

Figure 5.12: Whisker box plot of Phase variance for *E. coli-1*, *E. coli-2*, *K. pneumonia* and *S.aureus* (a) at 532 nm (b) at 660 nm.

5.2.11 Kurtosis

The average kurtosis decreased by 1.9% for *E. coli-1*, 1.21 % for *E. coli-2*, 0.096% for *K. pneumonia*, and 0.4% for *S.aureus* on increasing wavelength from 532nm to 660nm.

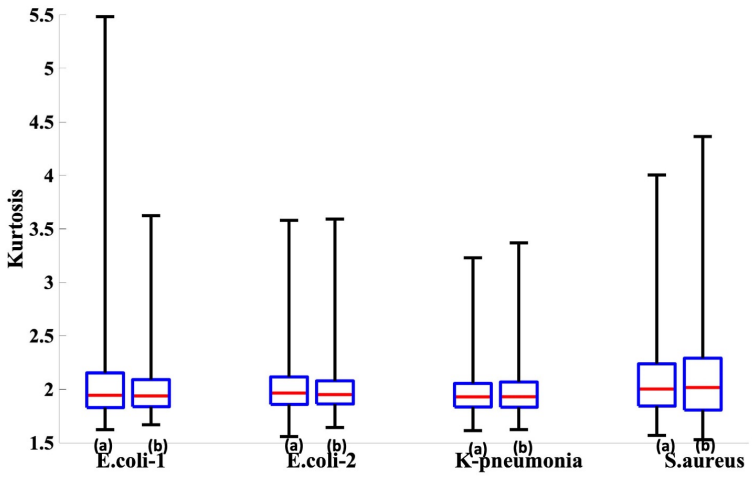

Figure 5.13: Whisker box plot of kurtosis for *E. coli-1*, *E. coli-2*, *K. pneumonia*and *S.aureus* (a) at 532nm (b) at 660nm. Median kurtosis remained the same for all bacteria cells. However, quartiles are changing slightly with the rose of wavelength.

5.2.12 Skewness

Skewness decreased by increasing the wavelength from 532 nm to 660 nm. It fell by 27.4% for *E. coli-1*, 30.01 % for *E. coli-2*, 16.4% for *K. pneumonia*, and 7.93% for *S.aureus* on switching wavelength from 532 nm to 660 nm.

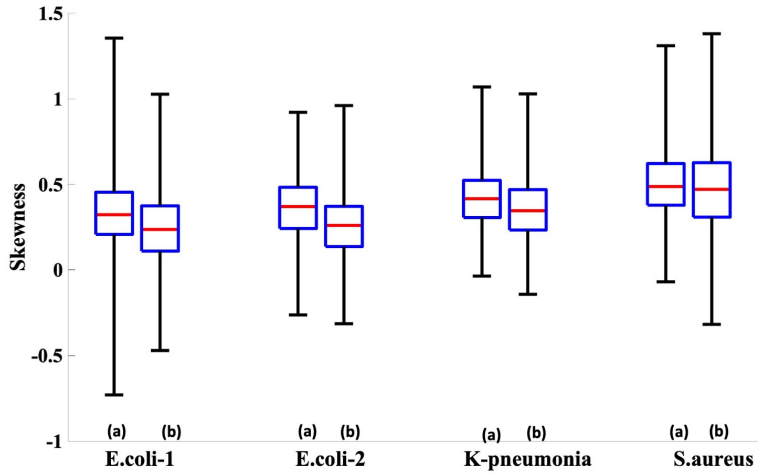

Figure 5.14: Whisker box plot of skewness for *E. coli-1*, *E. coli-2*, *K. pneumonia* and *S.aureus* (a) at 532nm (b) at 660nm. The median and quartiles of skewness decreased with the increase of wavelength.

5.2.13 Statistical significance and histogram

We utilized the two-sample t-test for the *p-values* of the data to analyze statistical differences across the bacteria cells, for derived morphological parameters of each bacteria cell at the single and dual wavelengths (532 nm and 660 nm). At first, we considered a single wavelength, i.e., 532nm. We took all the bacteria samples in a pair of two, e.g., *E. coli-1 and S. aureus*. In this way, we made six pairs of bacteria cells to check the statistical significance of their morphological parameters using the two-sample t-test.

Our null hypothesis was that mean of every morphological parameter was the same for both the bacteria cells at 532 nm. The alternative hypothesis was that there was a significant difference between the mean of morphological parameters for each bacteria cell at 532 nm. The threshold α for the t-test was 0.05. The histograms of all the parameters were plotted to check if the distribution of the sample is *gaussian* or not. Fig.5.15 shows the histograms plotted for all the morphological parameters of *E. coli-1* and *S. aureus*. The morphological parameters were significantly different and satisfied the alternative hypothesis. The symbol $***$ on the histograms in the Fig.5.15 represents $p<0.0005$. This process was repeated for all pairs of bacteria cells. In comparing all other pairs, i.e., *E. coli-1* and *S. aureus*, *K. pneumonia*, and *E. coli-2*, *E. coli-2*, and *S. aureus*, *K.pneumonia* and *S. aureus*, we found that nine morphological parameters were statistically significant. The figures are shown in *Appendix Section* to save space.

Then, the statistical significance of morphological parameters for dual-wavelength was checked using the same two-sample t-test. *The null hypothesis was that there is no change in the arithmetic mean of morphological parameters on changing the wavelength. The respective alternative hypothesis was that there is a significant change in the arithmetic*

Table 5.1: Morphological parameters (M.P) of four Bacteria cells at two different wavelengths (532 nm and 660 nm), i.e., surface area, volume,S/V, and sphericity correspondingto the experiment described in Section 4.1.

M.P		Bacteria							
		E.coli-1		*E.coli-2*		*K.pneumonia*		*S.aureus*	
		532 (nm)	660 (nm)	532 (nm)	660 (nm)	532 (nm)	660 (nm)	532 (nm)	660 (nm)
SA (μm^2)	Mean	8.9	8.6	6.8	7.1	7.2	7.2	8.3	8.3
	STD	1.9 ***	1.9	0.4 ***	1.4	1.8 -	1.8	1.9 -	1.9
PA(μm^2)	Mean	0.82	0.82	0.83	0.82	0.81	0.82	0.77	0.77
	STD	0.07-	0.07	0.08 -	0.08	0.08 *	0.09	0.07 -	0.07
V(μm^3)	Mean	0.1	0.1	0.1	0.1	0.1	0.1	0.2	0.2
	STD	0.05 ***	0.05	0.04 ***	0.04	0.06 ***	0.06	0.08 ***	0.09
SA/V (μm^{-1})	Mean	69	63	76	66	74	64	54	49
	STD	12 ***	10	13 ***	9	19 ***	14	14 ***	11
PA/V (μm^{-1})	Mean	6.8	6.3	9.9	8.2	9.3	8.1	5.5	4.9
	STD	2.5 ***	2.2	3.4 ***	2.6	4.3 ***	3.6	2.7 ***	2.2
Sphericity (ψ)	Mean	0.14	0.15	0.14	0.16	0.15	0.16	0.17	0.18
	STD	0.02 ***	0.01	0.01 ***	0.01	0.02 ***	0.02	0.02 ***	0.02
Energy	Mean	0.3	0.4	0.2	0.3	0.3	0.4	0.7	0.7
	STD	0.2 ***	0.2	0.2 ***	0.2	0.3 ***	0.3	0.6 *	0.6
Entropy	Mean	3.0	2.9	2.9	2.9	3.0	3.1	3.5	3.5
	STD	0.4 ***	0.4	0.4 *	0.3	0.5 -	0.5	0.5 **	0.5
Mean(μm) $*10^-2$	Mean	2.0	2.0	2.0	2.0	2.0	2.0	2.0	2.0
	STD	0.3 ***	0.3	0.3 ***	0.3	0.5 ***	0.4	0.6 ***	0.6
Variance(μm) $*10^-5$	Mean	9.5	8.1	8.1	7.1	12	11	26	22
	STD	6.5 ***	5.3	7.2 ***	5.1	1.1 *	9	25 ***	21
kurtosis	Mean	2.0	2.0	2.0	2.0	2.0	2.0	2.0	2.0
	STD	0.3 ***	0.2	0.2 *	0.2	0.2 -	0.2	0.3 -	0.3
Skewness	Mean	0.3	0.2	0.4	0.2	0.4	0.3	0.5	0.5
	STD	0.2 ***	0.2	0.2 ***	0.2	0.2 ***	0.2	0.2 ***	0.2

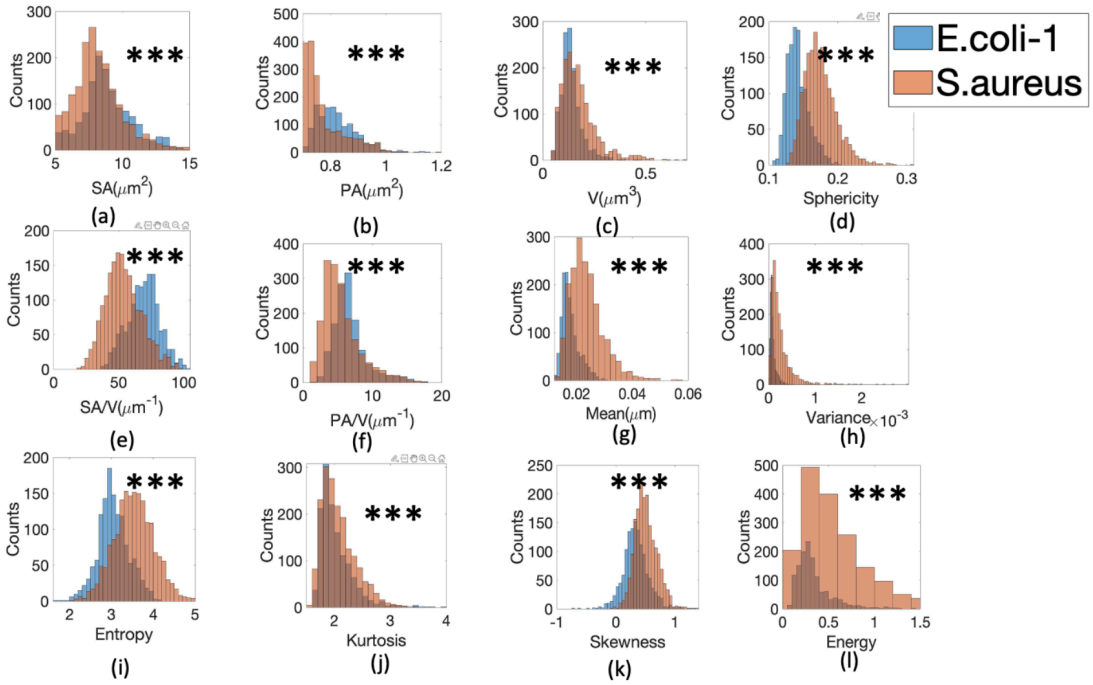

Figure 5.15: Histograms of the morphological parameters based the *OPD* maps for *E. coli-1* (blue) versus at *S.aureus* (brown): (a) surface area, (b) projected area, (c) phase volume, (d) sphericity, (e) phase surface area to volume ratio, (f) projected area to volume ratio, (g) variance, (h) mean, (i) entropy, (j)kurtosis, (k) skewness and (l) energy. *** denotes *P-values* <0.0005 – for $p>0.05$.

mean of morphological parameters on changing the wavelength. We repeated this process for all four bacteria cells. Fig.5.16 represents the corresponding histograms for *E. coli-1*, and *p-values* were represented by the * symbol on top of them. It was found that eight the morphological parameters satisfied the alternative hypothesis for all the morphological parameters. The histogram images are shown in *Appendix Section*. However, *Table 5.1* and symbol * describe the statistical significance at dual-wavelength.

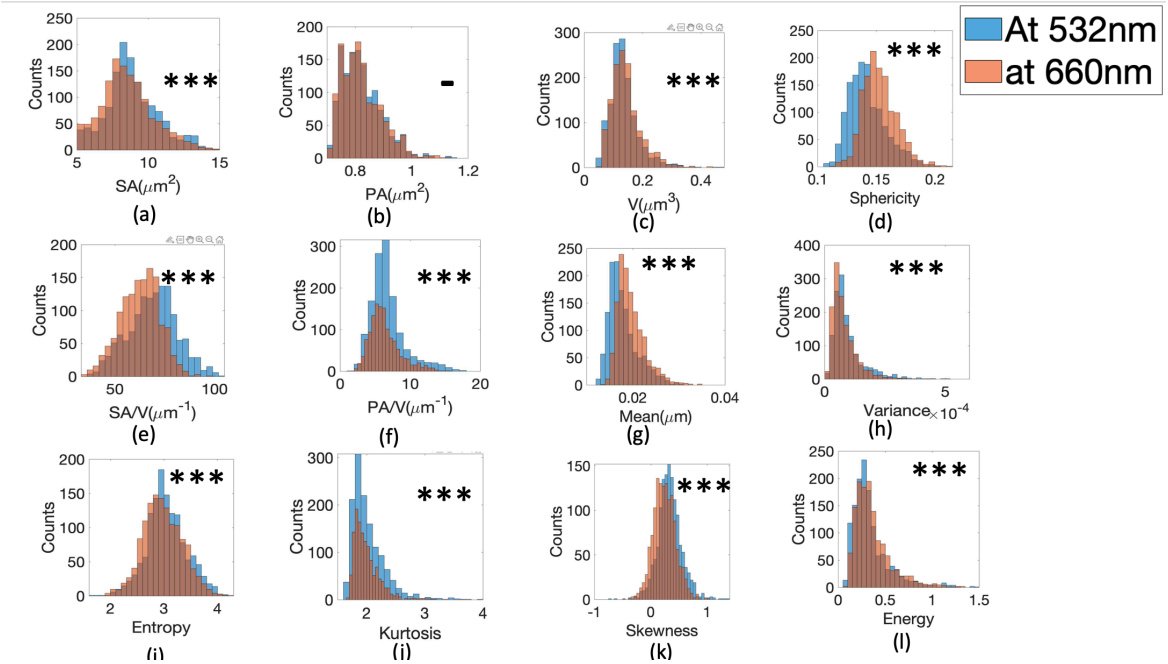

Figure 5.16: Histograms of the morphological parameters based on the *OPD* maps for *E. coli-1* at 532 nm (blue) versus at 660 nm (brown): (a) surface area, (b) projected area, (c) phase volume, (d) sphericity, (e) phase surface area to volume ratio, (f) projected area to volume ratio, (g) variance, (h) mean, (i) entropy, (j)kurtosis, (k) skewness and (l) energy. Symbol *** denotes *P-values* <0.0005 – for $p>0.05$.

5.3 Discussion

The primary hypothesis was to investigate any difference in the morphology and quantitative parameters obtained by the *QPM* images of four different bacterial cells (*E. coli-1*, *E. coli-2*, *K. pneumonia*, and *S. aureus*). In addition, we wanted to see if different bacteria cells could assign a unique fingerprint to distinguish them quickly using *QPI* and the measured morphological parameters. Fig.4.8 depicts different classes of bacteria cells, illustrating that a naked eye cannot detect significant differences even when utilizing QPI. However, the quantitative analysis of morphological parameters can solve this by studying the cell's *OPD* maps.

Table 5.1 summarizes the average and standard deviation values for each parameter for all cells. Quantitative analysis suggested that few morphological parameters were different on average at a single wavelength, including SA, SA/V, and PA/V. However, the wavelength has affected the estimation of numerous statistical parameters. Volume, sphericity, and energy increased while all other parameters decreased with an increase in a wavelength. As bacteria were attached to the substrate, the projected area of bacteria was not changing as a function of wavelength. The geometrical thickness should remain constant with a change in wavelength. The optical thickness changed as the refractive index changed with wavelength because the refractive index was changing, consequently, the phase.

Furthermore, increasing the wavelength surface area of all the bacteria cells decreased. In addition, we saw that when the wavelength was changed, the average projected area, kurtosis, and entropy of the cell's *OPD* did not change much, and minute changes were observed.

At a single wavelength(i.e., 532 nm), the *SA/V* and the *PA/V* were minima for *S.aureus* and maximum for *E. coli-2*. That was an exciting result as *SA/V* and *PA/V* of *non-AMR E. coli* (*E. coli-1*) was lower than *AMR E. coli* (*E. coli-2*). The *PA/V* and *SA/V* decreased with the increase of wavelength of light. The fall in the *projected area (PA)* and *surface area* (*SA*) on increasing the wavelength supported the rise in phase volume. Together, they were responsible for the overall decrease in surface area to volume ratio and projected area to volume ratio.

Sphericity was 0.142±0.0483 in the case of *E. coli-1*,0.144±0.0562 for *E. coli-2* and 0.148±0.0631 for *K. pneumonia* at a single wavelength, i.e., 532nm. Moreover, on increasing the wavelength, the sphericity index rose. The bacteria's phase maps were found to be higher at 532 nm than that for 660 nm and found to be in good agreement with the theory, which predicts an increase in refractive index when the wavelength falls.

Every statistical and morphological parameter followed a non-linear trend. Unfortunately, all statistical parameters overlap for the two wavelengths, making it challenging to build unique fingerprints of the bacteria cells using whisker box plots, mean, and standard deviations. It was logical that there was specific variation within bacteria, which was also highlighted by a relatively large spread in the morphological distributions for every sample.

At this point, we used the two-sample t-test for *p-values* to check in two ways
(1) If morphological parameters could differentiate bacteria cells at a single wavelength. First, we tested the bacteria cells in a pair of two bacteria cells. e.g. *E. coli-1 and E. coli-2* or *S.aureus and K.pneumonia*. In this, we make six pairs and test the significance of the results.
(2) If on changing the wavelength, the parameters were changing.

At a single wavelength, we did a two-sample t-test using all four samples in a pair of two at a threshold of 0.05. In comparing *E. coli-1* and *E. coli-2*, we found that all the parameters were statistically significant except kurtosis. For all the parameters, *p-values* were less than 0.0005. In the two-sample t-test between *E. coli-1* and *K. pneumonia*, the results of all the parameters were significant except mean and entropy. For all other pairs of bacteria cells (i.e., *E. coli-1* and *S.aureus*, *E. coli-2*, and *K. pneumonia*, *E. coli-2*, and *S.aureus* , *K. pneumonia* and *S. aureus*), the morphological parameters were significant with $p<0.0005$. Overall, 9 out of 12 parameters were significant at a single wavelength in all cases.

In the case of dual-wavelength, all the morphological parameters were statistically significant except the projected area for *E. coli-1* with $p<0.0005$. For *E. coli-2* projected area was not found to be statistically significant; entropy and kurtosis were found to be significant with $p<0.05$. All other parameters were significant. For *K. pneumonia*, all parameters

except surface area, entropy, and kurtosis were significantly different. In the case of *S.aureus*, all parameters except surface area, projected area, and kurtosis were quite different. Overall, eight out of 12 parameters were always significant with different probabilities. *Table 5.1* shows that 8 of the 12 *OPD*-based metrics were statistically significant. Every subfigure depicts the histograms of a particular parameter of bacteria cells. The results at two wavelengths were represented by different colors (blue for 532 nm and brown for 660 nm). Based on *p-values* of 0.05, 0.005, or 0.0005, all of these factors are statistically significant. These findings show that the parameters can statistically distinguish between each cell at two wavelengths, which was challenging to be done just using *OPD* analysis. The area under the curve values correlates to the separation between the groups shown in the histograms. (Fig.7.6 to Fig.7.8), with high percentages corresponding to lower *p-values* between the cells in the histograms. So volume, sphericity, *SA/V*, *PA/V*, mean, and skewness have a better separation than the rest of the parameters. If we combine all the results of a single wavelength and dual-wavelength, it was observed that 7 out of 12 parameters (i.e., volume, sphericity, *SA/V*, *PA/V*, variance, skewness, and energy) were significantly different in all the cases. Therefore, these seven parameters could be used in the future to build unique fingerprints of these bacteria cells.

In 2017, similar research distinguished cancer and healthy cells using morphological parameters. They found high statistical significance in the difference between the cell groups in most of the parameters estimated after evaluating tens of cells in each group, with the same patterns for all statistically significant parameters. Additionally, using the parameters and a machine learning system, diagnosis of the cell type (healthy/cancer/metastatic) was done with 81 to 93 percent sensitivity and 81 to 99 percent specificity [45].

In the future, deep learning approaches can be implemented to classify these bacteria samples for diagnostic purposes. The acquired seven overall statistically significant morphological parameters (V, SA/V, PA/V, sphericity, energy, variance, and skewness) and the machine-learning techniques can enable the establishment of unique fingerprints and quick identification of *AMR* bacteria cells.

Chapter 6

Conclusion

First, we systematically characterized the performance of the *QPM* system in terms of spatial and temporal phase sensitivity, spatial resolution, the effect of defocusing on the revered phase maps of the bacteria samples. Then, the spatial phase sensitivity of the setup is measured for direct *laser* and *PTLS* and compared. The system's phase sensitivity is 5.6mrad for *PTLS*, higher than for direct *laser*. Moreover, the temporal phase stability of the system is measured to be equal to 38 mrad, which is quite good and can utilize for the study of the dynamics of the cells.

Furthermore, it is observed that slight defocus in the recorded data introduces significant error in the recovered phase maps of the bacteria cells. Therefore, we numerically compensated its effect for generating accurate phase maps of the bacteria sample to analyze the morphological and statistical parameters further.

Moreover, the experiments are conducted with a diode laser of approximately 1 nm spectral bandwidths and an extremely narrow band (0.001 pm) laser. Due to its short temporal coherence length, a *diode laser* can only create circular fringes with high contrast. Furthermore, this led to circular fringe-like artifacts in the phase-shifting algorithm on recovered phase maps. The explanation behind the formation of such artifacts is the spatial frequency variation over the camera *FOV* when the shape of fringes is circular. A high-coherent laser can correct this sort of artifact, which generates straight fringes instead of circular fringes due to the possibility of an extended range of *OPD* adjustment.

For noise-free images, chromatic aberration-free optical components are required. A narrow-band light source such as a laser might bypass these restrictions; however, the high temporal coherence length increased the noise and lowered the spatial phase sensitivity. Therefore, a spatially low and temporally high coherent source (i.e., *PTLS*) can solve this problem.

This study employed *PTLS* based *QPM* to see the morphological differences between bacteria cells at a single wavelength. Unfortunately, all statistical parameters overlap on a single wavelength, making it challenging to build unique fingerprints of the bacteria cells.

Therefore, dual-wavelength *QPM* is used to extend the work and exploit the spectral diversity to develop new wavelength-dependent bio-markers and create a distinct boundary

between different bacteria samples. The bacteria's phase maps are found to be higher at 532 nm than that for 660 nm and found to be in good agreement with the theory, which predicts an increase in refractive index when the wavelength is decreased. Every statistical and morphological parameter follows a trend, but this trend is not linear. The aim was to investigate if different bacteria respond differently to the wavelength change. The refractive index is a function of wavelength. It was envisioned that other bacteria might react differently to a change of wavelength, which could be used as a biomarker to differentiate them. The two-sample t-test showed that for a single wavelength, nine out of 12, and for dual-wavelength, eight out of 12 parameters were significantly different. Combining the results showed that 7 out of 12 parameters (i.e., volume, sphericity, *SA/V*, *PA/V*, variance, skewness, and energy) were significantly different in all the cases.

In the future, these seven parameters and deep learning approaches can be implemented to classify these bacteria samples and build unique fingerprints for diagnostic purposes.

Chapter 7

Appendix

7.1 Statistical significance at single and dual wavelength

In this *Section*, histogram plots along with results of two sample t-test were shown. Nine out of 12 parameters satisfied the alternative hypothesis for single wavelength. Three morphological parameters including kurtosis, mean and entropy satisfied the null hypothesis in the following Fig.7.1, and Fig.7.2. The single wavelength results with were represented on the histograms Fig. 7.1 to Fig. 7.5 by symbol $*$ for $p<0.05$,$**$ for $p<0.005$,$***$ for $p<0.0005$ and $-$ for $p>0.05$.

Eight out of 12 parameters satisfied the alternative hypothesis for dual-wavelength. Four morphological parameters including surface area, projected area, entropy and kurtosis satisfied the null hypothesis. The results of dual wavelength are shown in Fig.7.6 to Fig.7.8.

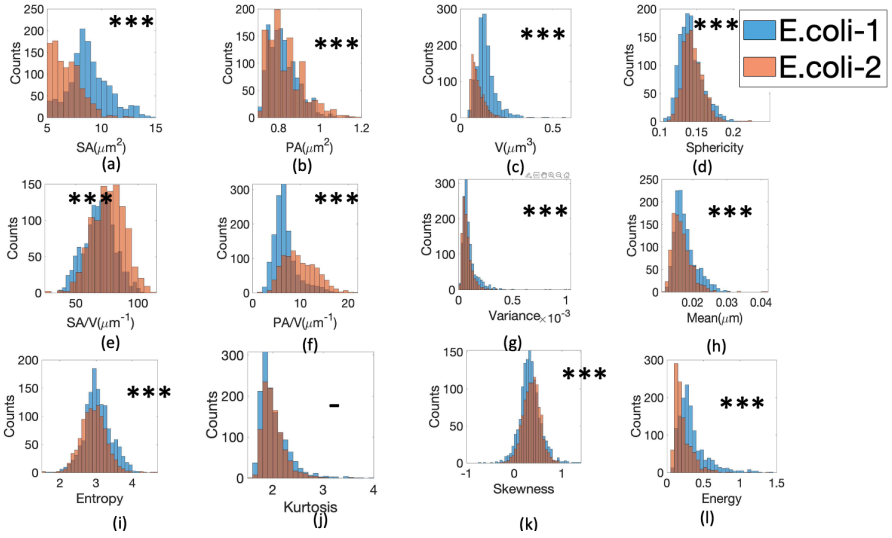

Figure 7.1: Histograms of the morphological parameters based the *OPD* maps for *E. coli-1* (blue) versus at *E. coli-2* (brown): (a) surface area, (b) projected area, (c) phase volume, (d) sphericity, (e) phase surface area to volume ratio, (f) projected area to volume ratio, (g) variance, (h) mean, (i) entropy, (j)kurtosis, (k) skewness and (l) energy.Symbol *** denotes *p-values <0.0005*.

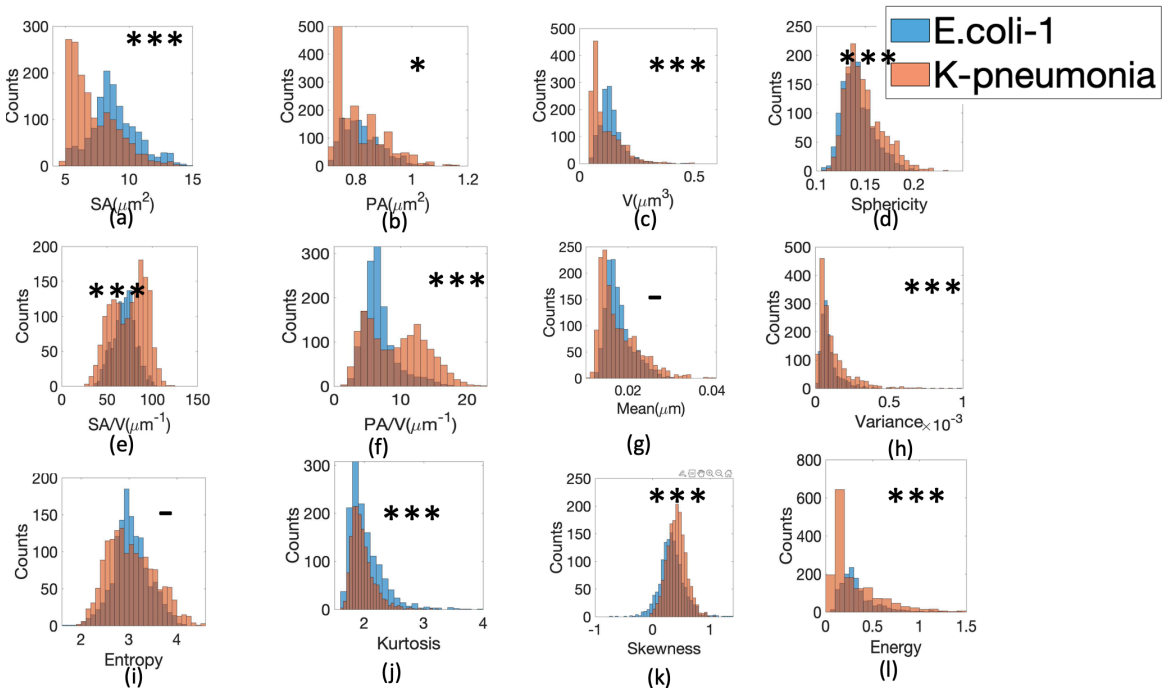

Figure 7.2: Histograms of the morphological parameters based the *OPD* maps for *E. coli-1* (blue) versus at *K .pneumonia* (brown): (a) surface area, (b) projected area, (c) phase volume, (d) sphericity, (e) phase surface area to volume ratio, (f) projected area to volume ratio, (g) variance, (h) mean, (i) entropy, (j)kurtosis, (k) skewness and (l) energy. Symbol * denotes *p-values <0.05* and *** denotes *p-values <0.0005*.

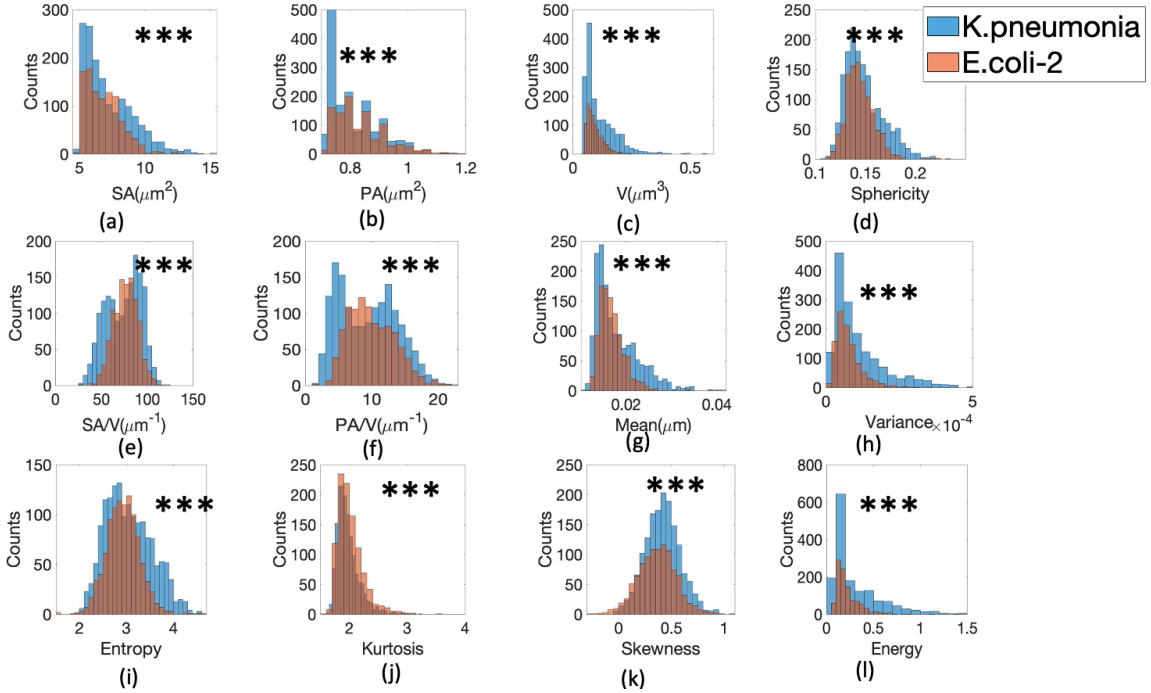

Figure 7.3: Histograms of the morphological parameters based the *OPD* maps for *K .pneumonia* (blue) versus at *E. coli-2* (brown): (a) surface area, (b) projected area, (c) phase volume, (d) sphericity, (e) phase surface area to volume ratio, (f) projected area to volume ratio, (g) variance, (h) mean, (i) entropy, (j)kurtosis, (k) skewness and (l) energy. Symbol *** denotes *p-values <0.0005*.

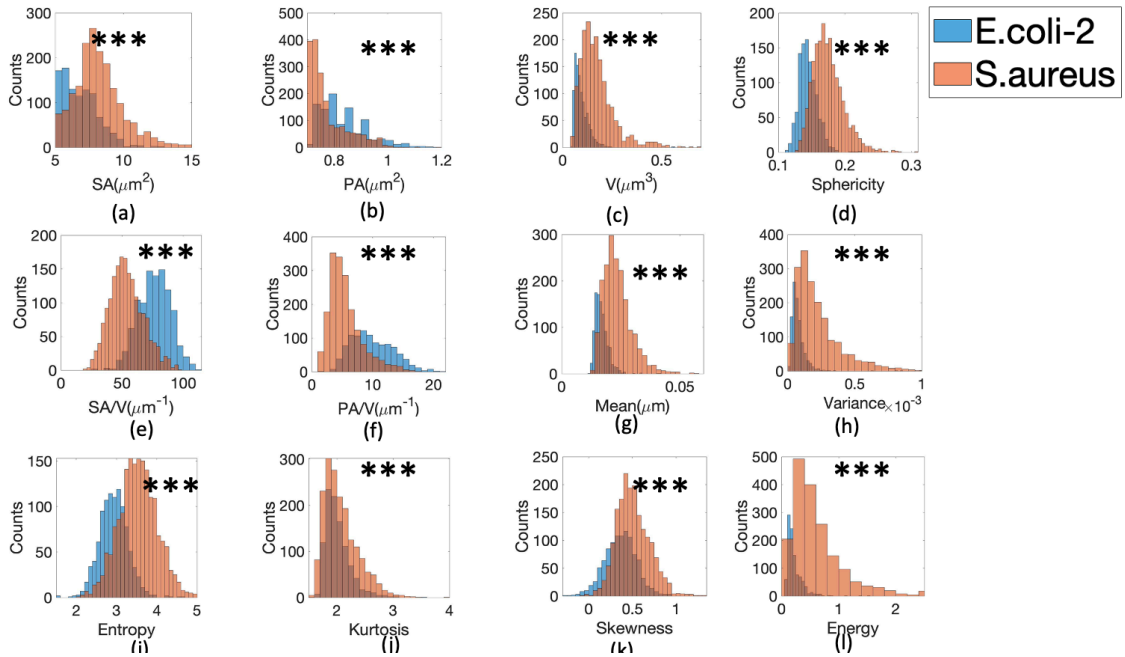

Figure 7.4: Histograms of the morphological parameters based the *OPD* maps for *E. coli-2* (blue) versus at *S .aureus* (brown): (a) surface area, (b) projected area, (c) phase volume, (d) sphericity, (e) phase surface area to volume ratio, (f) projected area to volume ratio, (g) variance, (h) mean, (i) entropy, (j)kurtosis, (k) skewness and (l) energy. Symbol *** denotes *p-values <0.0005*.

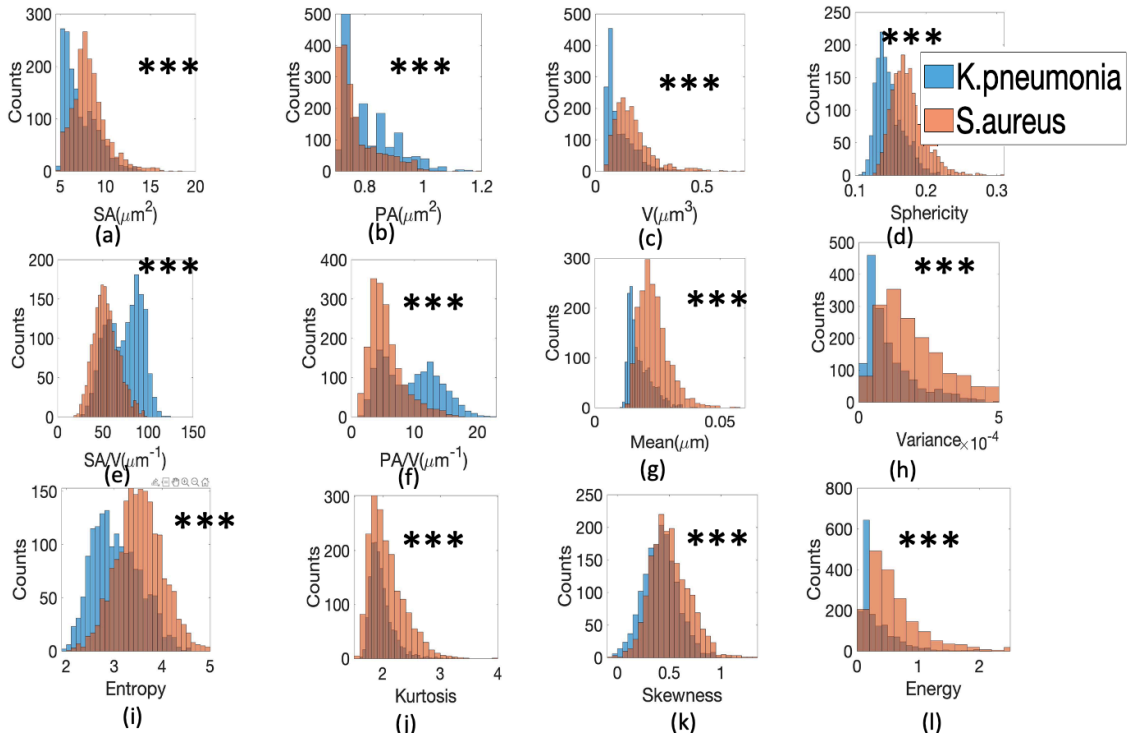

Figure 7.5: Histograms of the morphological parameters based the *OPD* maps for *K.pneumonia* (blue) versus at *S .aureus* (brown): (a) surface area, (b) projected area, (c) phase volume, (d) sphericity, (e) phase surface area to volume ratio, (f) projected area to volume ratio, (g) variance, (h) mean, (i) entropy, (j)kurtosis, (k) skewness and (l) energy. Symbol *** denotes *p-values <0.0005*.

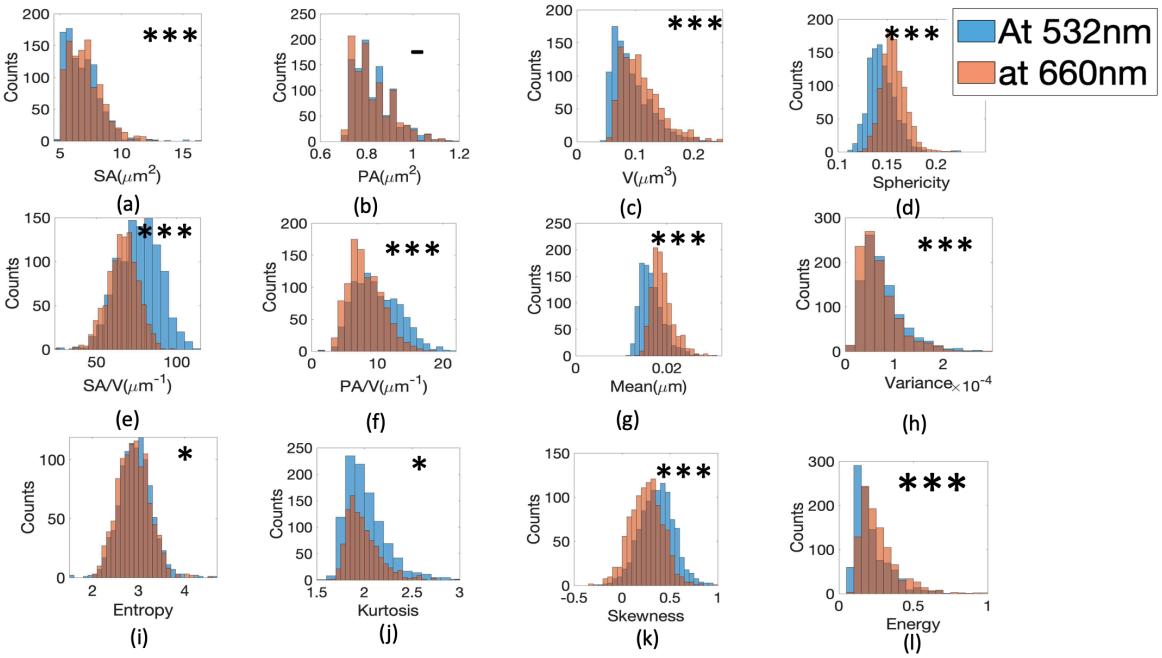

Figure 7.6: Histograms of the morphological parameters based the *OPD* maps for *E.coli-2* at 532nm(blue) versus at 660nm (brown): (a) surface area, (b) projected area, (c) phase volume, (d) sphericity, (e) phase surface area to volume ratio, (f) projected area to volume ratio, (g) mean, (h)variance, (i) entropy, (j)kurtosis, (k) skewness and (l) energy. Symbol * denotes *p-values <0.05* and *** denotes *p-values <0.0005*.

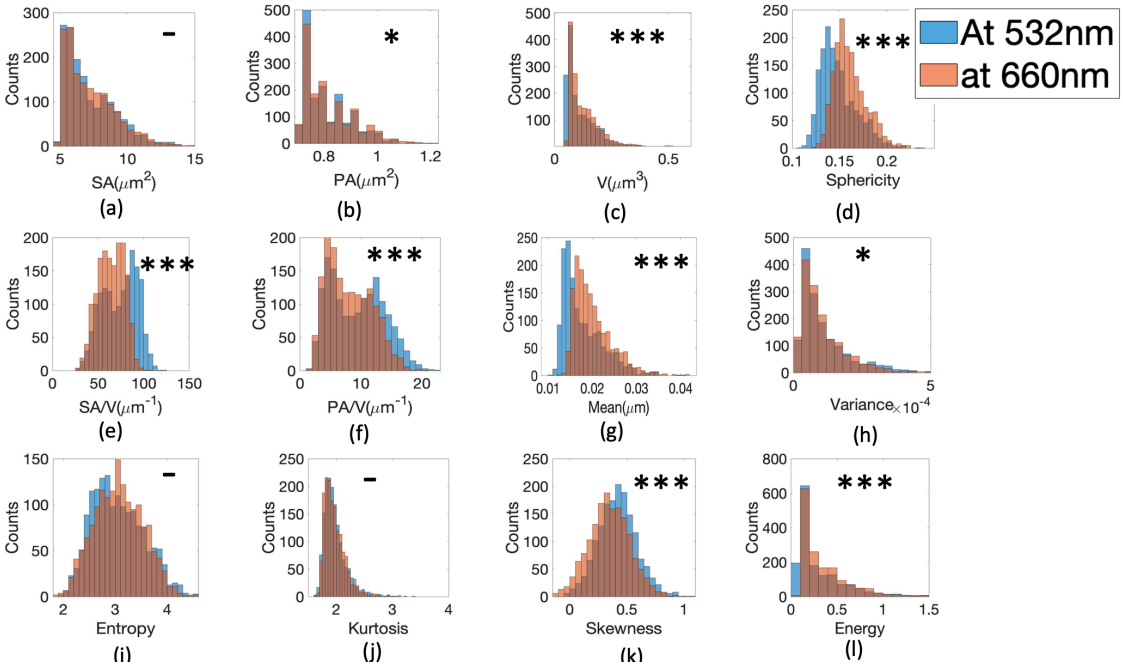

Figure 7.7: Histograms of the morphological parameters based the *OPD* maps for *K.pneumonia*at 532nm(blue) versus at 660nm (brown): (a) surface area, (b) projected area, (c) phase volume, (d) sphericity, (e) phase surface area to volume ratio, (f) projected area to volume ratio, (g) mean, (h)variance, (i)entropy, (j)kurtosis, (k) skewness and (l) energy.Symbol * denotes *p-values <0.05* and *** denotes *p-values <0.0005*.

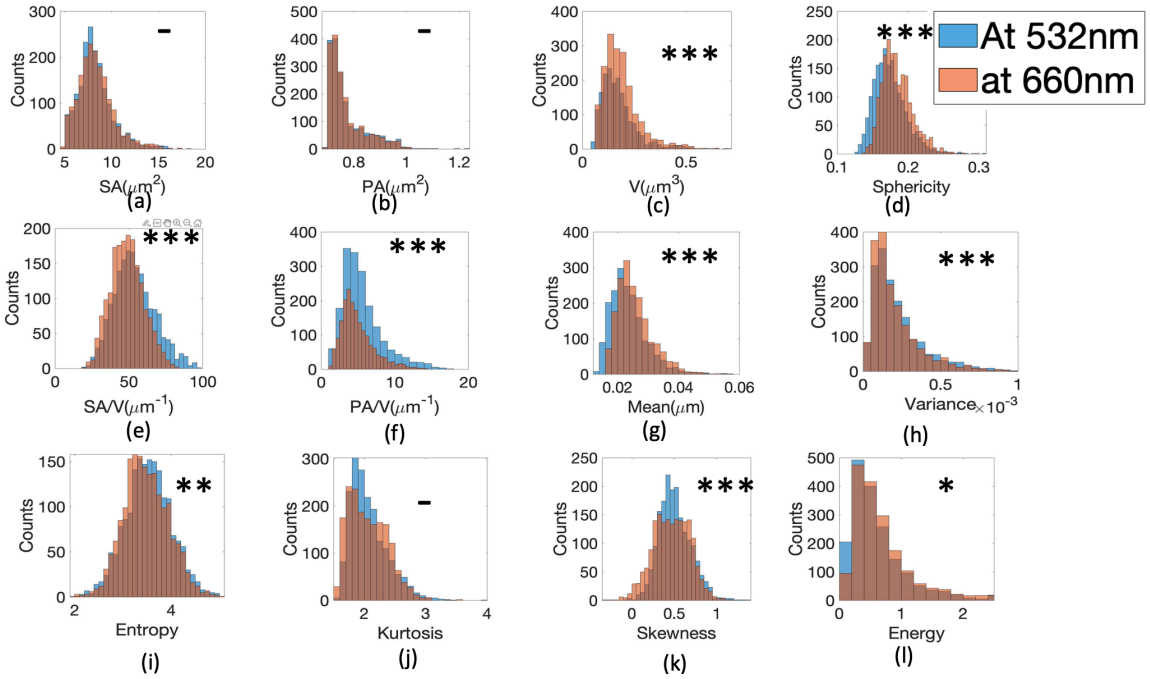

Figure 7.8: Histograms of the morphological parameters based the *OPD* maps for *S.aureus* at 532nm(blue) versus at 660nm (brown): (a) surface area, (b) projected area, (c) phase volume, (d) sphericity, (e) phase surface area to volume ratio, (f) projected area to volume ratio, (g) Mean, (h)variance, (i) entropy, (j)kurtosis, (k) skewness and (l) energy.Symbol * denotes *p-values <0.05* and *** denotes *p-values <0.0005*.

Bibliography

[1] The American Society for Microbiology and NIH. Basic Research on Bacteria. The essential Frontier, 2007.

[2] https://www.who.int/news-room/fact-sheets/detail/antimicrobial-resistance

[3] Avershina E, Sharma P, Taxt AM, Singh H, Frye SA, Paul K, Kapil A, Naseer U, Kaur P, Ahmad R. AMR-Diag: Neural network based genotype-to-phenotype prediction of resistance towards β-lactams in Escherichia coli and Klebsiella pneumoniae. Computational and structural biotechnology journal. 2021 Jan 1;19:1896-906.

[4] https://www.researchgate.net/publication/326518972 Quantitative Phase Microscopy and Tomography with Spatially Incoherent Light

[5] Antimicrobial Resistance: Tackling a Crisis for the Health and Wealth of Nations: December 2014, author=Review on Antimicrobial Resistance (London). and Grande-Bretagne, year=2014, publisher=Review on antimicrobial resistance

[6] Anti-virulence Therapy Targeting Staphylococcus Aureus, author=Baldry, Mara, year=2016, publisher=Department of Veterinary Disease Biology, University of Copenhagen

[7] Phase imaging with computational specificity (PICS) for measuring dry mass changes in sub-cellular compartments, author=Kandel, Mikhail E and He, Yuchen R and Lee, Young Jae and Chen, Taylor Hsuan-Yu and Sullivan, Kathryn Michele and Aydin, Onur and Saif, M Taher A and Kong, Hyunjoon and Sobh, Nahil and Popescu, Gabriel, journal=Nature communications, volume=11, number=1, pages=1–10, year=2020, publisher=Nature Publishing Group

[8] Popescu G. Quantitative phase imaging of cells and tissues. New York etc.: McGraw-Hill; 2011.

[9] Ahmad, Azeem & Dubey, Vishesh & Jayakumar, Nikhil & Habib, Anowarul & Butola, Ankit & Nystad, Mona & Acharya, Ganesh & Basnet, Purusotam & Mehta, Dalip & Ahluwalia, Balpreet. (2020). High throughput spatially sensitive single-shot quantitative phase microscopy.

[10] I. Abdulhalim, Spatial and temporal coherence effects in interference microscopy and fullfield optical coherence tomography, Annalen der Physik, Vol. 524, 2012, pp. 787-804.

[11] L. Mandel, E. Wolf, Optical Coherence and Quantum Optics, Cambridge University Press,1995.

[12] V. Ryabukho, D. Lyakin, A. Grebenyuk, S. Klykov, Wiener–Khintchin theorem for spatial coherence of optical wave field, Journal of Optics, Vol. 15, 2013, 025405.

[13] Ghatak AK, Thyagarajan K, Tiyākarācan K. Optical electronics: Cambridge University Press; 1989

[14] https://www3.nd.edu/ amoukasi/CBE30361/Useful

[15] R. Guo et al., "Off-axis digital holographic microscopy with LED illumination based on polarization filtering," Appl. Opt., 52 (34), 8233 –8238 (2013). https://doi.org/10.1364/AO.52.008233 APOPAI 0003-6935 Google Scholar

[16] V. Dubey, D. Popova, A. Ahmad, G. Acharya, P. Basnet, D. S. Mehta, and B. S. Ahluwalia, "Partially spatially coherent digital holographic microscopy and machine learning for quantitative analysis of human spermatozoa under oxidative stress condition," Sci. Rep. 9(1), 1–10 (2019).

[17] Jo Y, Jung J, Kim M-h, Park H, Kang S-J, Park Y. Label-free identification of individual bacteria using Fourier transform light scattering. Optics express. 2015;23(12):15792-805.

[18] Ahmad A, Srivastava V, Dubey V, Mehta DS. Ultra-short longitudinal spatial coherence length of laser light with the combined effect of spatial, angular, and temporal diversity. Applied Physics Letters. 2015 Mar 2;106(9):093701.

[19] Ahmad A, Dubey V, Singh VR, Tinguely J-C, Øie CI, Wolfson DL, et al. Quantitative phase microscopy of red blood cells during planar trapping and propulsion. Lab on a Chip. 2018;18(19):3025-36.

[20] A. Ahmad, T. Mahanty, V. Dubey, A. Butola, B. S. Ahluwalia, and D. S. Mehta, "Effect on the longitudinal coherence properties of a pseudothermal light source as a function of source size and temporal coherence," Opt. Lett. 44(7), 1817–1820 (2019).

[21] V. Dubey, A. Ahmad, R. Singh, D. L.Wolfson, P. Basnet, G. Acharya, D. S. Mehta, and B. S. Ahluwalia, "Multi-modal chip-based fluorescence and quantitative phase microscopy for studying inflammation in macrophages," Opt. Express 26(16), 19864–19876 (2018).

[22] A. Dubois et al., “High-resolution full-field optical coherence tomography with a Linnik microscope,” Appl. Opt., 41 (4), 805 –812 (2002). https://doi.org/10.1364/AO.41.000805 APOPAI 0003-6935 Google Scholar

[23] N. Jayakumar et al., “Sampling Moiré method: a tool for sensing quadratic phase distortion and its correction for accurate quantitative phase microscopy,” Opt. Express, 28 (7), 10062 –10077 (2020). https://doi.org/10.1364/OE.383461 OPEXFF 1094-4087 Google Scholar

[24] Nadeau J, Cho YB, El-Kholy M, Bedrossian M, Rider S, Lindensmith C, et al., editors. Holographic microscopy for 3D tracking of bacteria. Quantitative Phase Imaging II; 2016: International Society for Optics and Photonics

[25] Ahmad A, Dubey V, Butola A, Ahluwalia BS, Mehta DS. Highly temporal stable, wavelength-independent, and scalable field-of-view common-path quantitative phase microscope. Journal of Biomedical Optics. 2020 Nov;25(11):116501.

[26] Chao, Y., Zhang, T. Optimization of fixation methods for observation of bacterial cell morphology and surface ultrastructures by atomic force microscopy. Appl Microbiol Biotechnol 92, 381–392 (2011). https://doi.org/10.1007/s00253-011-3551-5

[27] Popescu G, Kim T. Quantitative phase imaging of cells in 2-, 3-and 4-D. Optics and Photonics News. 2014;25(12).

[28] Bedrossian M, El-Kholy M, Neamati D, Nadeau J. A machine learning algorithm for identifying and tracking bacteria in three dimensions using Digital Holographic Microscopy. AIMS Biophysics. 2018.

[29] Yoon J, Lee K, Park Y. A simple and rapid method for detecting living microorganisms in food using laser speckle decorrelation. arXiv preprint arXiv:160307343. 2016.

[30] Nadeau JL, Cho YB, Kühn J, Liewer K. Improved tracking and resolution of bacteria in holographic microscopy using dye and fluorescent protein labeling. Frontiers in chemistry. 2016;4:17.

[31] Zaraee N, Kanik FE, Bhuiya AM, Gong ES, Geib MT, □UnIu NL, et al., editors. Highly Sensitive and Label-free Digital Detection of Whole Cell E. coli with Interferometric Reflectance Imaging (Conference Presentation). Label-free Biomedical Imaging and Sensing (LBIS) 2020; 2020: International Society for Optics and Photonics.

[32] Oh J, Ryu JS, Lee M, Jung J, Han S, Chung HJ, et al. Three-dimensional label-free observation of individual bacteria upon antibiotic treatment using optical diffraction tomography. Biomedical Optics Express. 2020;11(3):1257-67.

[33] Roitshtain D, Wolbromsky L, Bal E, Greenspan H, Satterwhite LL, Shaked NT. Quantitative phase microscopy spatial signatures of cancer cells. Cytometry A. 2017 May;91(5):482-493. doi: 10.1002/cyto.a.23100. Epub 2017 Apr 20. PMID: 28426133.

[34] Takeda M, Ina H, Kobayashi S. Fourier-transform method of fringe-pattern analysis for computer-based topography and interferometry. Journal of the Optical Society of America. 1982;72(1):156.

[35] Ahmad A, Dubey V, Butola A, Tinguely J-C, Ahluwalia BS, Mehta DS. Sub-nanometer height sensitivity by phase shifting interference microscopy under environmental fluctuations. Optics Express. 2020;28(7):9340-58.

[36] Hariharan P, Oreb B, Eiju T. Digital phaseshifting interferometry: a simple errorcompensating phase calculation algorithm. Applied optics 1987;26(13):25046.

[37] P. Hariharan, B. Oreb, and T. Eiju, "Digital phase-shifting interferometry: a simple error-compensating phase calculation algorithm," Appl. Opt. 26(13), 2504–2506 (1987).

[38] Vargas, Javier & Quiroga, J & Belenguer, Tomas. (2011). Analysis of the principal component algorithm in phase-shifting interferometry. Optics letters. 36. 2215-7. 10.1364/OL.36.002215.

[39] Wang, Zhaoyang & Han, Bongtae. (2004). Advanced iterative algorithm for phase extraction of randomly phase-shifted interferograms. Optics letters. 29. 1671-3. 10.1364/OL.29.001671.

[40] https://www.ccug.se/strain?id=17620

[41] Taxt AM, Avershina E, Frye SA, Naseer U, Ahmad R. Rapid identification of pathogens, antibiotic resistance genes and plasmids in blood cultures by nanopore sequencing. Scientific reports. 2020 May 6;10(1):1-1.

[42] https://www.phe-culturecollections.org.uk/products/bacteria/detail.

[43] https://www.ccug.se/strain?id=35600

[44] Kawagishi, Norikazu & Kakinuma, Ryota & Yamamoto, Hirotsugu. (2020). Aerial image resolution measurement based on the slanted knife edge method. Optics Express. 28. 35518. 10.1364/OE.408983.

[45] Peña-Cruz, Manuel Arancibia-Bulnes, Camilo , Abdul-Rahman, Hussein. (2012). FRINGE REFLECTION TECHNIQUE FOR HELIOSTATS, A COMPARISON BETWEEN TWO PHASE RETRIEVAL METHODS.

[46] Wadell H. Volume, shape, and roundness of quartz particles. J Geol 1935;43: 250–280.

[47] Porter PK. Allometry of mammalian cellular oxygen consumption. Cell Mol Life Sci 2001;58:815–822.

[48] https://en.wikipedia.org/wiki/1951 USAF resolution test chart

[49] Pham HV, Bhaduri B, Tangella K, Best-Popescu C, Popescu G. Real time blood testing using quantitative phase imaging. PLoS ONE 2013;8:e55676.

[50] Canham BP, Burton AC. Distribution of size and shape in populations of normal human red cells. Circ Res 1968;22:405–422.

[51] Mir M, Wang Z, Tangella K, Popescu G. Diffraction phase cytometry: Blood on a CD-ROM. Opt Express 2009;17:2579–2585.

[52] Rohila, Ashish & Sharma, Ambalika. (2019). Phase entropy: a new complexity measure for heart rate variability. Physiological Measurement. 40. 10.1088/1361-6579/ab499e.

[53] Dennis C. Ghiglia and Louis A. Romero, ”Minimum Lp-norm two-dimensional phase unwrapping,” J. Opt. Soc. Am. A 13, 1999-2013 (1996)